AMERICAN SOCIETY FOR MICROBIOLOGY | Journal of Virology®

VIRUS-CELL INTERACTIONS

Distinctive Roles of Furin and TMPRSS2 in SARS-CoV-2 Infectivity

Rachid Essalmani,[a] Jaspreet Jain,[b] Delia Susan-Resiga,[a] Ursula Andréo,[a,b] Alexandra Evagelidis,[a] Rabeb Mouna Derbali,[a] David N. Huynh,[a] Frédéric Dallaire,[b] Mélanie Laporte,[b] Adrien Delpal,[c] Priscila Sutto-Ortiz,[c] Bruno Coutard,[d] Claudine Mapa,[e] Keith Wilcoxen,[e] Etienne Decroly,[c] Tram NQ Pham,[b] Éric A. Cohen,[b,f] Nabil G. Seidah[a]

[a]Laboratory of Biochemical Neuroendocrinology, Montreal Clinical Research Institute (IRCM), Montreal, Quebec, Canada
[b]Laboratory of Human Retrovirology, Montreal Clinical Research Institute (IRCM), Montreal, Quebec, Canada
[c]AFMB, CNRS, Aix-Marseille University, CNRS, UMR 7257, Case 925, Marseille, France
[d]Unité des Virus Émergents (UVE), Aix-Marseille University, IRD 190, INSERM 1207, IHU Méditerranée Infection, Marseille, France
[e]Boston Pharmaceuticals, Translational Research, Cambridge, Massachusetts, USA
[f]Department of Microbiology, Infectiology and Immunology, Université de Montréal, Montreal, Quebec, Canada

Jaspreet Jain, Delia Susan-Resiga, and Ursula Andréo contributed equally to this article. Author order was determined by the names was based on the importance of the contribution of each author.

ABSTRACT The spike protein (S) of severe acute respiratory syndrome coronavirus 2 (SARS-CoV-2) directs infection of the lungs and other tissues following its binding to the angiotensin-converting enzyme 2 (ACE2) receptor. For effective infection, the S protein is cleaved at two sites: S1/S2 and S2′. The "priming" of the surface S protein at S1/S2 (P**R**RA**R**$_{685}$↓) [the underlined basic amino acids refer to critical residues needed for the furin recognition] by furin has been shown to be important for SARS-CoV-2 infectivity in cells and small-animal models. In this study, for the first time we unambiguously identified by proteomics the fusion activation site S2′ as KPS**KR**$_{815}$↓ (the underlined basic amino acids refer to critical residues needed for the furin recognition) and demonstrated that this cleavage was strongly enhanced by ACE2 engagement with the S protein. Novel pharmacological furin inhibitors (BOS inhibitors) effectively blocked endogenous S protein processing at both sites in HeLa cells, and SARS-CoV-2 infection of lung-derived Calu-3 cells was completely prevented by combined inhibitors of furin (BOS) and type II transmembrane serine protease 2 (TMPRSS2) (camostat). Quantitative analyses of cell-to-cell fusion and S protein processing revealed that ACE2 shedding by TMPRSS2 was required for TMPRSS2-mediated enhancement of fusion in the absence of S1/S2 priming. We further demonstrated that the collectrin dimerization domain of ACE2 was essential for the effect of TMPRSS2 on cell-to-cell fusion. Overall, our results indicate that furin and TMPRSS2 act synergistically in viral entry and infectivity, supporting the combination of furin and TMPRSS2 inhibitors as potent antivirals against SARS-CoV-2.

IMPORTANCE SARS-CoV-2, the etiological agent of COVID-19, has so far resulted in >6.1 million deaths worldwide. The spike protein (S) of the virus directs infection of the lungs and other tissues by binding the angiotensin-converting enzyme 2 (ACE2) receptor. For effective infection, the S protein is cleaved at two sites: S1/S2 and S2′. Cleavage at S1/S2 induces a conformational change favoring the S protein recognition by ACE2. The S2′ cleavage is critical for triggering membrane fusion and virus entry into host cells. Our study highlights the complex dynamics of interaction between the S protein, ACE2, and the host proteases furin and TMPRSS2 during SARS-CoV-2 entry and suggests that the combination of a nontoxic furin inhibitor with a TMPRSS2 inhibitor significantly reduces viral entry in lung cells, as evidenced by an average synergistic ~95% reduction of viral infection. This represents a powerful novel antiviral approach to reduce viral spread in individuals infected by SARS-CoV-2 or future related coronaviruses.

Editor Mark T. Heise, University of North Carolina at Chapel Hill

Address correspondence to Éric A. Cohen, eric.cohen@ircm.qc.ca, or Nabil G. Seidah, seidahn@ircm.qc.ca.

The authors declare no conflict of interest.

Received 24 January 2022
Accepted 1 March 2022
Published 28 March 2022

KEYWORDS Calu-3 cells, furin, HeLa cells, SARS-CoV-2, spike, TMPRSS2, viral entry, viral infection, cell-to-cell fusion

Severe acute respiratory syndrome coronavirus (SARS-CoV-1) and Middle East respiratory syndrome coronavirus (MERS-CoV) are infectious pathogenic viruses that appeared in humans at the beginning of the 21st century (1, 2). At the end of 2019, a third CoV, namely, SARS-CoV-2, emerged, causing widespread respiratory and vascular illnesses (3) coined COVID-19 (4).

Like envelope glycoproteins of many infectious viruses (5–7), the secretory type-I membrane-bound spike (S) protein of SARS-CoV-2 is synthesized as a precursor (proS) that undergoes posttranslational cleavages by host cell proteases at specific sites to allow viral entry. During infection, the trimeric proS (monomer, 1,273 residues) is first processed at an S1/S2 cleavage site (Fig. 1A). Unlike SARS-CoV-1, the S protein of SARS-CoV-2 exhibits an insertion of four critical amino acids (PRRA) at the S1/S2 junction (8–10), forming a canonical P**R**RA**R**$^{685}\downarrow$ furin-like cleavage site (FCS) (8). Such a "priming" step divides the protein into two subunits, S1 and S2, held together by noncovalent interactions. Various reports have since supported the implication of furin in the S1/S2 priming of the S protein in human cell culture models (10–12) and *in vivo* in mice, hamsters, and ferrets (12, 13). Following S protein priming, the S1 ectodomain undergoes a conformational change that exposes its receptor-binding domain (RBD) (14), which recognizes the angiotensin-converting enzyme 2 (ACE2) entry receptor (9). The S2 subunit, which is responsible for the fusogenic activity of the S glycoprotein, contains an additional "fusion activation" proteolytic site (S2′) followed by an α-helical fusion peptide (FP) and two heptad repeat domains (HR1 and HR2) preceding the transmembrane domain (TM) and cytosolic tail (CT) (Fig. 1A). It is thought that cleavage at S2′ triggers large-scale protein rearrangements, including a refolding step that is associated with the separation of the S1 and S2 subunits and exposure of the hydrophobic α-helix FP, thus favoring fusion of viral and host cell membranes and leading to virus entry (15). Fusion with host cells can occur either at the cell surface (pH independent) or with internal membranes following endocytosis (pH dependent) (16). However, the cognate host cell proteases responsible for the S1/S2 and S2′ cleavages vary between coronaviruses and cell types (9, 10, 17–20).

The proprotein convertases (PCs; genes *PCSK*s) constitute a family of nine secretory serine proteases that regulate various processes in both health and disease states (21). Through proteolysis, PCs are responsible for the activation and/or inactivation of many secretory precursor proteins, including virus/pathogen surface glycoproteins (7, 21). Seven PCs, including the widely expressed furin, PC5A, PACE4, and PC7, cleave secretory substrates at specific single/paired basic amino acids within the motif (K/R)-X_n-(K/R)$\downarrow$, where X_n represents 0, 2, 4, or 6 spacer X residues (21). Because of their critical functions, PCs, especially furin (22), are implicated in many viral infections by inducing specific cleavages of envelope glycoproteins, a condition that not only allows fusion of the viral lipid envelope with host cell membranes (7, 21) but also can lead to cell-to-cell fusion (syncytia), especially for viruses that undergo pH-independent fusion (23, 24).

Based on the predicted S2′ site at the KPS**KR**$_{815}\downarrow$S**F** sequence of SARS-CoV-2, we proposed that furin-like enzymes could also cleave at this putative S2′ site (Fig. 1A) (8). In addition, it was also suggested that the cell surface type II transmembrane serine protease 2 (TMPRSS2) can enhance fusion by facilitating cleavage at S2′. The ability of the Arg/Lys-specific TMPRSS2 (25, 26) to directly cleave at S2′ was suggested based on the viral entry blockade by the TMPRSS2 inhibitor camostat (27–29) and on the silencing of TMPRSS2 expression using a morpholino oligomer (19), but direct evidence of TMPRSS2 involvement in such spike protein processing at S2′ is still lacking. Thus, it is likely that one or more proteases regulate SARS-CoV-2 entry into human airway epithelial cells (19, 30). Furthermore, since the tissue expression of TMPRSS2 is restricted to a limited set of cell types compared to that of the ubiquitously expressed furin, the activity of the latter may widen viral tropism (31).

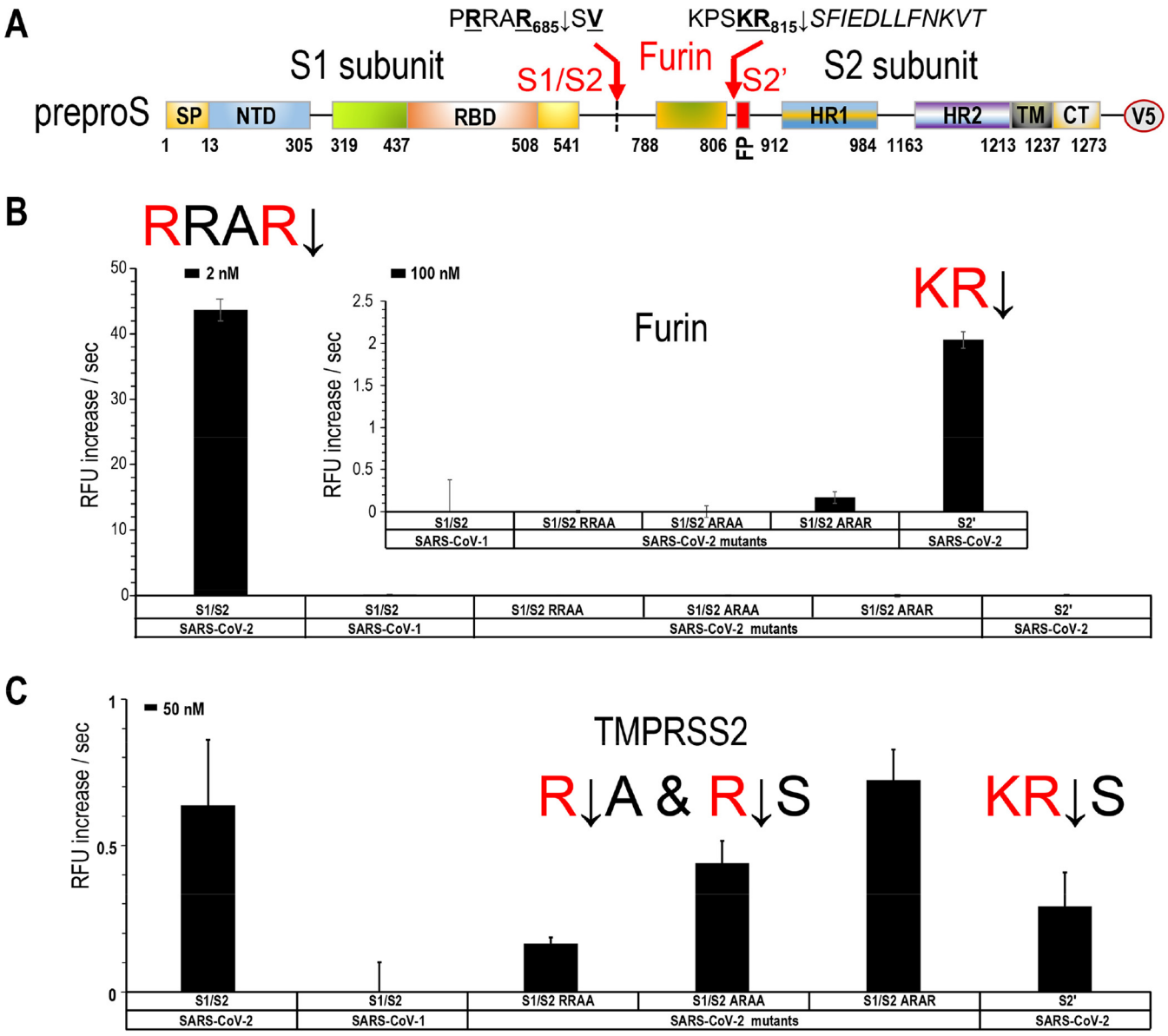

FIG 1 Processing of S peptides by furin and TMPRSS2. (A) Schematic representation of the primary structure of preproS, including its domains, the predicted furin-like S1/S2 site generating the S1 and S2 subunits, and the S2′ site preceding the fusion peptide (FP). The signal peptide (SP), N-terminal domain (NTD), receptor binding domain (RBD) to ACE2, the two heptad repeats HR1 and HR2, the transmembrane domain (TM), the cytosolic tail (CT), and the C-terminal V5 tag are indicated. (B) *In vitro* furin activity against peptides mimicking the S1/S2 (and its mutants) and S2′ cleavage site sequences of the spike protein from SARS-CoV-2 and SARS-CoV-1, as described in Table 1. Each substrate was tested at final protease concentrations of 2 and 100 nM. (C) *In vitro* TMPRSS2 activity (at 50 nM) against peptides mimicking the indicated S1/S2 and S2′ cleavage site sequences as described in Table 1.

The major goals of the present study were to precisely define the respective roles of furin and TMPRSS2 in fusion activation and to test the consequences of their inhibition on SARS-CoV-2 infectivity and S-mediated cell-to-cell fusion. In this study, using a multidisciplinary approach, we obtained mechanistic evidence supporting a critical role of the proprotein convertase furin in the processing of SARS-CoV-2 spike protein. Specifically, we mapped the exact S2′ processing site by proteomics and highlighted by mutagenesis the functional importance of the S1/S2 and S2′ regions in viral entry and cell-to-cell fusion. For the first time, we demonstrate that three novel cell-permeable nonpeptide small-molecule inhibitors of the proprotein convertases (BOS inhibitors) can potently inhibit proS processing at both S1/S2 and S2′ by endogenous furin-like proteases and thus lead to efficient inhibition of viral entry, viral replication, and cell-to-cell

TABLE 1 Sequences of peptides mimicking the SARS-CoV spike cleavage sites[a]

Peptide	S1/S2 site	S2′ site
SARS-CoV-1 (WT)	YHTVSLLR ↓ $STSQ_{671}$	
SARS-CoV-2 (WT)	TNSPRRAR ↓ $SVAS_{689}$	$SKPSKR↓SFIE_{819}$
SARS-CoV-2 S1/S2 RRAA	$TNSPRRAASVAS_{689}$	
SARS-CoV-2 S1/S2 ARAA	$TNSPARAASVAS_{689}$	
SARS-CoV-2 S1/S2 ARAR	$TNSPARARSVAS_{689}$	
SARS-CoV-2 S2′ RRKR		$SKRRKRSFIE_{819}$

[a]The arrow indicates the expected cleavage site.

fusion. Finally, our work highlights the importance of ACE2 for enhancing S2′ processing by furin and TMPRSS2 and of TMPRSS2 shedding of ACE2 for increasing cell-to-cell fusion.

RESULTS

Cleavage of SARS-CoV-2 peptides mimicking S1/S2 and S2′ processing sites by furin and TMPRSS2: a comparative analysis. Furin is thought to be important in the processing of SARS-CoV-2 spike glycoprotein (S) at the S1/S2 site (8, 30), while TMPRSS2 has been proposed to have an important role in activating S at S2′ (19, 27–29) (Fig. 1A). Nevertheless, the relative contributions of furin and TMPRSS2 toward cleavage of SARS-CoV-2 S glycoprotein at both sites remain poorly defined. Thus, the susceptibility of SARS-CoV-2 S glycoprotein to furin cleavage was first assessed *in vitro*. Incubation of quenched fluorogenic peptides encompassing S1/S2 and S2′ sites (Table 1) demonstrated that the S1/S2 site of SARS-CoV-2 S was efficiently cleaved by 2 nM furin at pH 7.5 (Fig. 1B), whereas the S1/S2 site of SARS-CoV-1, which lacks an FCS, was not cleaved (Fig. 1B). In contrast, furin was less effective at cleaving at S2′, requiring 50-fold-higher enzyme concentrations (inset in Fig. 1B). The high specificity of the SARS-CoV-2 for processing at furin-like motifs was next confirmed by demonstrating that substitutions of basic residues at the S1/S2 cleavage site (RRA$\underline{\mathbf{A}}_{685}$↓S, $\underline{\mathbf{A}}$RA$\underline{\mathbf{A}}_{685}$↓S, and $\underline{\mathbf{A}}$RAR_{685}↓S) dramatically impaired S1/S2 cleavage (Fig. 1B). Together, these data demonstrate that *in vitro* furin cleaves best at S1/S2 and less efficiently at S2′. In contrast, TMPRSS2 did not efficiently cleave the SARS-CoV-2 S1/S2 and S2′ peptides (Fig. 1C), requiring a 50 nM concentration. However, in contrast to furin, TMPRSS2 cleavages of Ala mutant peptides RRA$\underline{A}$, $\underline{A}$RA$\underline{A}$, and $\underline{A}$RAR mimicking the S1/S2 and S2′ sites were detectable under this condition (Fig. 1C). Taken together, these data emphasize the critical importance of the P1 and P4 Arg for furin-mediated cleavage at S1/S2 and suggest that the likely Arg motif recognized by TMPRSS2 is either (Ala/Arg)-Arg↓Ala or Ala-Arg↓Ser, with a preference for Ala at P2 over Arg and for Ala or Ser at the residue following the cleavage site (P1′).

Furin and furin-like proteases can process proS at S1/S2 and S2′ sites. To examine the ability of furin and furin-like enzymes to process the precursor proS of SARS-CoV-2 *in cellulo*, we used HeLa cells, which endogenously express furin but not TMPRSS2 or ACE2, as reported earlier (32). In this study, we found that an endogenous enzyme(s) efficiently processed a V5-tagged proS (Fig. 1A), likely at the S1/S2 junction, to generate an ~100-kDa S2-like fragment (Fig. 2A). Of note, a knockdown of endogenous furin decreased S2 levels by more than 60% (Fig. 3A). Furthermore, overexpressed furin or PC5A, but not PC7 or PACE4 (all expressed at similar mRNA levels; see quantitative reverse transcription-PCR [qPCR] data), cleaved proS at a potential S2′ site, yielding an ~75-kDa fragment (Fig. 2A). The remaining ~200-kDa $proS_{im}$ corresponded to an immature precursor form that had not exited the endoplasmic reticulum (ER), as attested by its sensitivity to both endoglycosidase F (endo-F) and endoglycosidase H (endo-H) (Fig. 3B) and insensitivity to furin-like convertases, which are only active in the *trans*-Golgi network (TGN) and/or cell surface/endosomes (21, 33).

To precisely define the ~100-kDa fragment, we mutated the S1/S2 site $\underline{\mathbf{R}}$RA$\underline{\mathbf{R}}_{685}$↓S and found that the double Ala mutant [$\underline{\mathbf{A}}$RA$\underline{\mathbf{A}}_{685}$] (designated μS1/S2) abrogated processing at S1/S2 and putative S2′ (Fig. 2B), highlighting once again the importance of

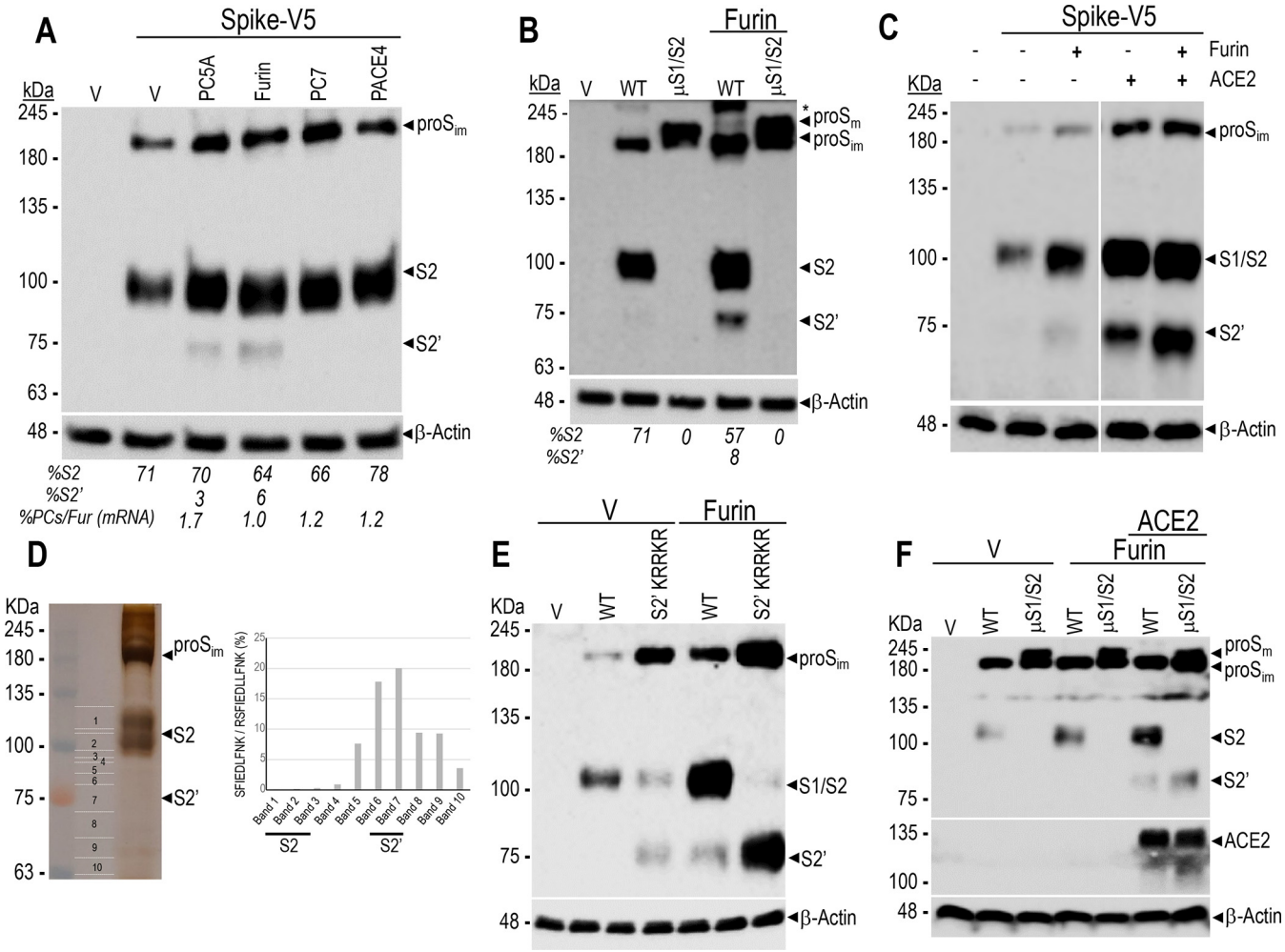

FIG 2 Processing of spike glycoprotein in HeLa cells and critical role of ACE2. (A) Western blot analyses of the processing of WT proS into V5-tagged S2 and S2′ by the proprotein convertases furin, PC5A, PACE4, and PC7 following cotransfection of their cDNAs in HeLa cells. The migration positions of immature $proS_{im}$, S2, and S2′ as well as the actin loading control are emphasized. V, empty pIRES-EGFP-V5 vector. The estimated percent cleavages into S1/S2 and S2′ are shown and were calculated as the ratio of the V5 immunoreactivity of the cleaved form to the sum of all forms. As estimated by qPCR, the percent mRNA levels of overexpressed PCs relative to furin are also shown. The data are representative of those from at least three independent experiments. (B) Western blot analyses of HeLa cells following cotransfection with cDNAs coding for either WT S protein (WT) or its double Ala mutant (R685A + R682A) (μS1/S2) in the absence or presence of furin cDNA at a ratio of S to protease of 1:2. *, inconsistently observed oligomeric forms of proS. (C) Western blot analyses of HeLa cells cotransfected with V5-tagged spike protein, WT S or its furin-optimized S2′ ($KRRKR_{815}\downarrow SF$) mutant (μS2′), and empty vector (V) or furin. (D) Identification of S2′ cleavage site by tandem mass spectrometry (MS/MS). WT spike glycoprotein was immunoprecipitated from HeLa cells using V5-agarose beads, then resolved by SDS-PAGE, and subjected to silver staining (left side); the positions of the slices are indicated (1 to 10). The MS/MS analysis of peptides generated by a Lys-specific protease (K814↓) is indicated; the data represent the ratio of $SFIEDLLFNK_{825}$ to $R_{815}SFIEDLLFNK_{825}$ (right side). (E and F) Western blot showing the impact of ACE2 on the processing of WT and μS1/S2 spike glycoproteins by furin. HeLa cells expressing empty vector, WT proS, or its μS1/S2 mutant with or without furin, ACE2, or both were analyzed by Western blotting using anti-V5 antibody. The ratio of cDNAs used was 1:1:1 for S, ACE2, and furin. The data are representative of those from at least three independent experiments.

the positions of P4 and P1 Arg for recognition by furin-like enzymes (21). Expression of μS1/S2 demonstrated the loss of furin-like cleavage at S1/S2 in the spike protein and the accumulation of a higher-molecular-weight band (~230 kDa), representing mature $proS_m$ (Fig. 2B) that exited the ER, as confirmed by its resistance to endoglycosidase H and sensitivity to endoglycosidase F digestion (Fig. 3B).

To further define the Arg residues critical for processing at S1/S2, we assessed the effect of single-residue mutations R682A, R685A, and S686A and confirmed the necessity of P1 Arg_{685} or P4 Arg_{682} for the generation of S2 by endogenous furin (Fig. 3C). However, unlike μS1/S2 (Fig. 2B), these single mutants were partially cleaved by overexpressed furin (Fig. 3C), reflecting the multibasic nature of the S1/S2 recognition sequence and possibly revealing the importance of the P3 Arg_{683} (34). The S686A mutant was generated on the prediction that Ser_{686} could be O-glycosylated (35), which

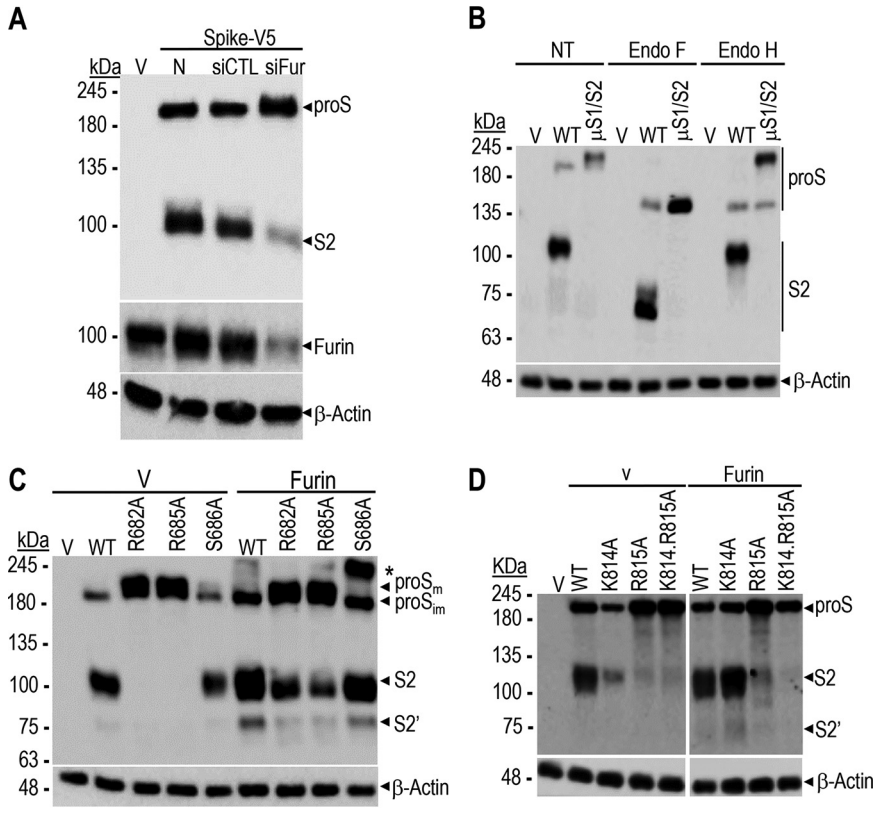

FIG 3 Importance of furin in the processing of the spike glycoprotein. (A) HeLa cells were first transfected with control nontargeting siRNA (siCTL) or siRNA furin (siFur) at a final concentration of 20 nM, or mock transfected (N), and 24 h later, transfected with empty vector or with that coding for a V5-tagged spike glycoprotein for an additional 48 h. Following lysis, proteins were resolved by SDS-PAGE followed by WB with anti-V5 or anti-furin antibodies. (B) HeLa cells transfected with empty vector, V5-tagged WT spike protein, or its S1/S2 site mutant (μS1/S2) were treated with endoglycosidase F (endo-F) and endoglycosidase H (endo-H) or mock treated (NT) and analyzed as described for panel A. (C and D) HeLa cells transfected with V5-tagged wild-type spike protein or S1/S2 single mutants (C) or S2′ single or double mutants (D) in the absence (V) or presence of overexpressed furin were lysed and analyzed by WB.

may hamper processing at S1/S2 (36). However, like the wild-type (WT) S, the S686A mutant was efficiently processed by furin into S2 and S2′ (Fig. 3C).

We next attempted to use site-directed mutagenesis to identify the exact S2′ site cleaved by furin. However, K814A, R815A, and K814R815A mutations at P1 or/and P2 residues of the predicted S2′ site (KPS$\underline{KR}_{815}\downarrow$SF) dramatically altered S protein trafficking and resulted in a predominantly ER-retained $proS_{im}$ protein, especially for the R815A mutant and the double mutant, which were resistant to furin cleavage (Fig. 3D). It is important to note that the recently reported loss of processing at S2′ of a similar R815A S protein led to the erroneous suggestion that prior cleavage at S1/S2 is not needed for S2′ processing (37), as these authors did not analyze the ER retention, and hence resistance to furin cleavage, of such a proS R815A mutant. To precisely identify the S2′ site, we resorted to mass spectrometry analysis of proteins migrating at the S2′ position. The peptides generated by a Lys-specific protease ($K_{814}\downarrow$) allowed for discrimination between SFIEDLLFN$\underline{K}_{825}$, which would be produced if furin cleaved at Arg_{815}, and $\underline{R}_{815}$SFIEDLLFN$\underline{K}_{825}$, which would be derived from N-terminally extended proteins, e.g., S2. Proteomic data (Fig. 2C) revealed a >50-fold-higher ratio of $\underline{S}$FIEDLLFN$\underline{K}_{825}$ to $\underline{R}$SFIEDLLFN$\underline{K}_{825}$ for the S2′ product, demonstrating that the N terminus of S2′ starts at Ser_{816} and that furin cleaves after $Arg_{815}\downarrow$ in the sequence KPSK$\underline{R}_{815}\downarrow$SFIEDLLFNK (Fig. 1A). To further demonstrate the role of furin in S2′ cleavage, we generated a furin-optimized S2′ site (called μS2′) with a polybasic sequence, K$\underline{RR}$K$R_{815}\downarrow$SF, in proS and found that this variant was very efficiently cleaved by endogenous and especially by

overexpressed furin, yielding a similar ~75-kDa fragment (Fig. 2D). Together, these data demonstrate that indeed the S2′ cleavage occurs at $Arg_{815}\downarrow$ and further reveal that this site can be partially processed by overexpressed furin and/or PC5A.

Processing at S2′ by furin is enhanced in the presence of ACE2. Given that binding of SARS-CoV-2 S trimer to the dimeric ACE2 receptor has been proposed to trigger a conformational change in S1 and thus promote cleavage at S2′ (14, 38), we next examined whether this phenomenon would effectively increase/promote S2′ processing by furin. To this end, we expressed the V5-tagged proS spike protein together with human ACE2 and furin in HeLa cells. While still allowing for maximal S1/S2 cleavage, based on the absence of the mature $proS_m$ form (Fig. 2B), ACE2 expression seemed to stabilize the S2 subunit and to strongly enhance the generation of S2′ by endogenous and overexpressed furin (Fig. 2E). Amazingly, in the presence of ACE2 and overexpressed furin, μS1/S2-S, which was otherwise resistant to cleavage at S1/S2 by endogenous or overexpressed furin (Fig. 2B), could now be partially cleaved directly into S2′ (Fig. 2F, last lane). We conclude that binding of S protein to ACE2 likely facilitates exposure of the S2′ site (39), thereby enhancing furin processing at S2′.

Furin inhibitors block S1/S2 and S2′ cleavages. Given the importance of furin in proS processing at the S1/S2 and S2′ sites, we next evaluated the activity of three novel nontoxic, cell-permeative furin-like inhibitors developed by Boston Pharmaceuticals and available as oral (BOS-981 and BOS-318) or inhalable (BOS-857) formulations (Fig. 4A). Accordingly, we first tested *in vitro* the efficacy and selectivity of these inhibitors on purified soluble forms of furin, PC5A, PACE4, and PC7 using a quenched fluorogenic substrate, 6-carboxyfluorescein (FAM)–QRVRRAVGIDK–6-carboxytetramethylrhodamine (TAMRA). As shown in Fig. 4B, the inhibitors effectively blocked substrate processing by all convertases, with an half-maximal inhibitory concentration (IC_{50}) of ~7 to 9 nM, compared to ~9 to 10 nM for the known cell-permeative PC inhibitor decanoyl-RVKR-chloromethylketone (dec-RVKR-cmk) (40, 41). The furin S1/S2 cleavage was also validated using a 12-residue quenched fluorogenic substrate, DABSYL/Glu-TNSPRRAR$\downarrow$SVAS-EDANS, mimicking the S1/S2 priming site of SARS-CoV-2. The inhibition deduced after Hill plot curve fitting (Fig. 4C) gave estimated IC_{50}s of 4 $\pm$ 0.7 nM for BOS-981, 32 $\pm$ 4 nM for BOS-857, and 35 $\pm$ 5 nM for BOS-318. As well, BOS inhibitors inhibited endogenous furin-like processing of a dibasic bone morphogenic protein 10 (BMP10) mimic (41) with an IC_{50} of ~8 nM, versus 5 nM for the dec-RVKR-cmk, as determined by a cell-based Golgi imaging assay with U2OS cells (Fig. 4D). Finally, we showed that BOS inhibitors efficiently blocked S1/S2 and S2′ processing by endogenous furin-like enzymes in HeLa-ACE2 cells, resulting in a near complete inhibition at 0.3 μM. This inhibitory profile was also observed with 50 μM dec-RVKR-cmk (RVKR; Fig. 4E). Overall, our data clearly demonstrate that pharmacological inhibition of furin abrogates the processing of proS at the S1/S2 and S2′ sites in the HeLa cell model.

Furin-like inhibitors reduce virus production in SARS-CoV-2-infected cells. We next examined whether blocking of the processing of proS by BOS inhibitors modulates SARS-CoV-2 infection. Indeed, in lung-derived Calu-3 cells pretreated with 1 μM BOS inhibitors for 24 h before infection, we observed significantly decreased viral titers at 12, 24, and 48 h postinfection (Fig. 5A). Importantly, the inhibitory effect was dose dependent, reducing viral burden more than 30-fold with 1 μM BOS-318 (Fig. 5B, left). As well, the IC_{50} and selectivity index (42) of BOS-318 were 0.2 μM and 475, respectively (Fig. 5B, right). Notably, the levels of spike (full length and cleaved S) and nucleocapsid (N) proteins in the supernatant and cells were decreased in a dose-dependent manner (Fig. 5C), underscoring the important contribution of furin-like convertases in SARS-CoV-2 infection in Calu-3 cells. A similar analysis with BOS-857 and BOS-981 revealed comparable antiviral effects and selectivity indices (Fig. 6). In addition, BOS inhibitors were also evaluated in Vero E6 cells, in which SARS-CoV-2 entry and infection are established primarily via the endocytic pathway (9, 30). In this system and as expected, treatment with BOS inhibitors led to a modest effect, since we observed that virus production decreased only ~2.6- to 5.7-fold (Fig. 7), possibly reflecting a role of furin-like activity in early endosomes (33) for pH-dependent virus entry in Vero cells.

A

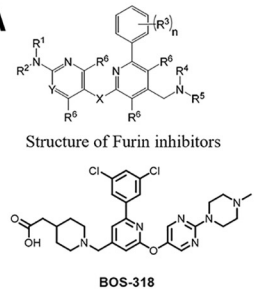

B

	Furin pIC50	PC5 pIC50	PACE4 pIC50	PC7 pIC50
BOS-318	8.8±0.4 (n=10)	6.7±0.15 (n=8)	6.7±0.15 (n=6)	7.4±0.22 (n=8)
BOS-981	9.3±0.5 (n=10)	7.5±0.22 (n=10)	6.9±0.1 (n=4)	6.9±0.2 (n=8)
BOS-857	9.4±0.3 (n=10)	7.6±0.2 (n=10)	6.7±0.24 (n=5)	6.9±0.3 (n=8)
decanoyl-RVKR-cmk	9.1±0.43 (n=447)	9.9±0.38 (n=162)	9.2±0.24 (n=214)	9.6±0.63 (n=198)

D

	Golgi pIC50 (U20S)
BOS-318	7.7±0.24 (n=22)
BOS-981	8.3±0.25 (n=12)
BOS-857	7.6±0.2 (n=12)
decanoyl-RVKR-cmk	5.1±0.33 (n=8)

C

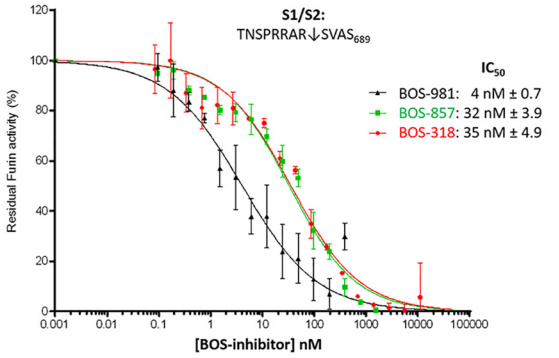

E

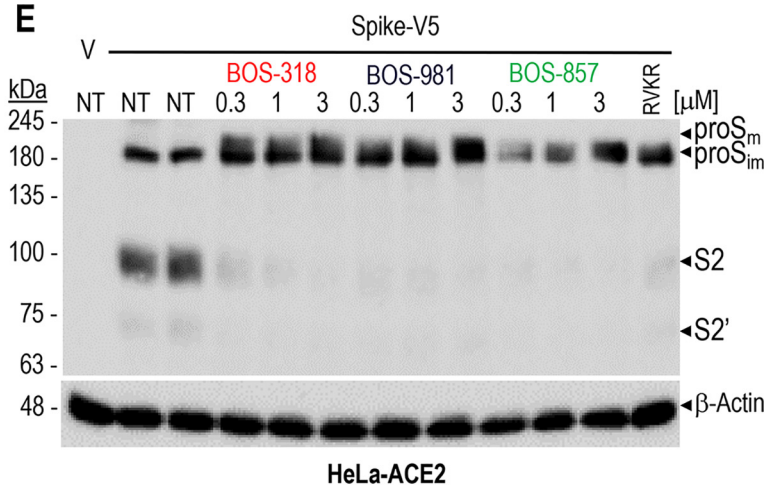

FIG 4 Inhibition of PCs by BOS compounds. (A) Chemical motif of BOS inhibitors and representative structure of BOS-318. (B) *In vitro* BOS inhibition of the cleavage of the fluorogenic dibasic substrate FAM-QRVRRAVGIDK-TAMRA by each of the proprotein convertases furin, PC5 (PCSK5), PACE4 (PCSK6), and PC7 (PCSK7). All experiments were performed in 10 different wells, and the average pIC_{50} (nanomolar) was calculated. Shown for comparison is the inhibitory pIC_{50} negative log of the IC_{50} value when converted to molar) of the furin-like inhibitor RVKR-cmk; determination was performed >100 times. (C) *In vitro* inhibition of furin by the BOS compounds. Furin (2 nM) was incubated with increasing concentration of BOS inhibitors, and its enzymatic activity against the synthetic peptides DABSYL/Glu-TNSP**RR**A**R**↓SVAS-EDANS (5 μM) was measured at pH 7.5 (n = 3). (D) Golgi assay; the table presents the effects of BOS inhibitors on U2OS cells expressing each of furin, PC5A, PACE4, and PC7 simultaneously transduced with a BacMam-delivered construct containing a Golgi-targeting sequence followed by a 12-amino-acid furin/PCSK cleavage site from bone morphogenic protein 10 (BMP10) and GFP at the C terminus (GalNAc-T2-GGGGS-DSTARIRR↓NAKG-GGGGS-GFP). Dibasic cleavage releases NAKG-GGGGS-GFP, thereby reducing the Golgi-associated fluorescence estimated by imaging. (E) Furin inhibitors (BOS) abrogate endogenous processing of the spike glycoprotein. HeLa-ACE2 cells were transiently transfected with a cDNA encoding an empty vector or with one expressing the V5-tagged spike glycoprotein (spike-V5). At 5 h pretransfection, cells were treated with the vehicle DMSO (NT, duplicate), with the furin inhibitors at the indicated concentrations, or with RVKR-cmk at 50 μM. At 24 h posttransfection, media were replaced with fresh ones lacking (NT) or containing the inhibitors for an additional 24 h. Cell extracts were analyzed by Western blotting using MAb V5. All data are representative of those from at least three independent experiments.

Since TMPRSS2 has been proposed to be important for viral entry at the plasma membrane, we next assessed whether combining BOS inhibitors and the TMPRSS2-inhibitor camostat would lead to a more pronounced antiviral effect in Calu-3 cells. As shown in Fig. 5D, although these compounds could reduce viral replication individually, their cotreatment resulted in a synergistic reduction of progeny infectious viruses of more than 70-fold, reinforcing the importance of both furin-like proteases and TMPRSS2 in promoting efficient SARS-CoV-2 infection of Calu-3 cells.

Furin-like inhibitors reduce viral entry by blocking processing of proS during biosynthesis and at the viral entry site. The more dramatic impact observed with furin-like inhibitors on virus infection of Calu-3 cells versus Vero cells suggests that these inhibitors affect mainly the pH-independent entry mechanism. Thus, we next assessed the effect of BOS inhibitors on viral entry. Using nanoluciferase-expressing

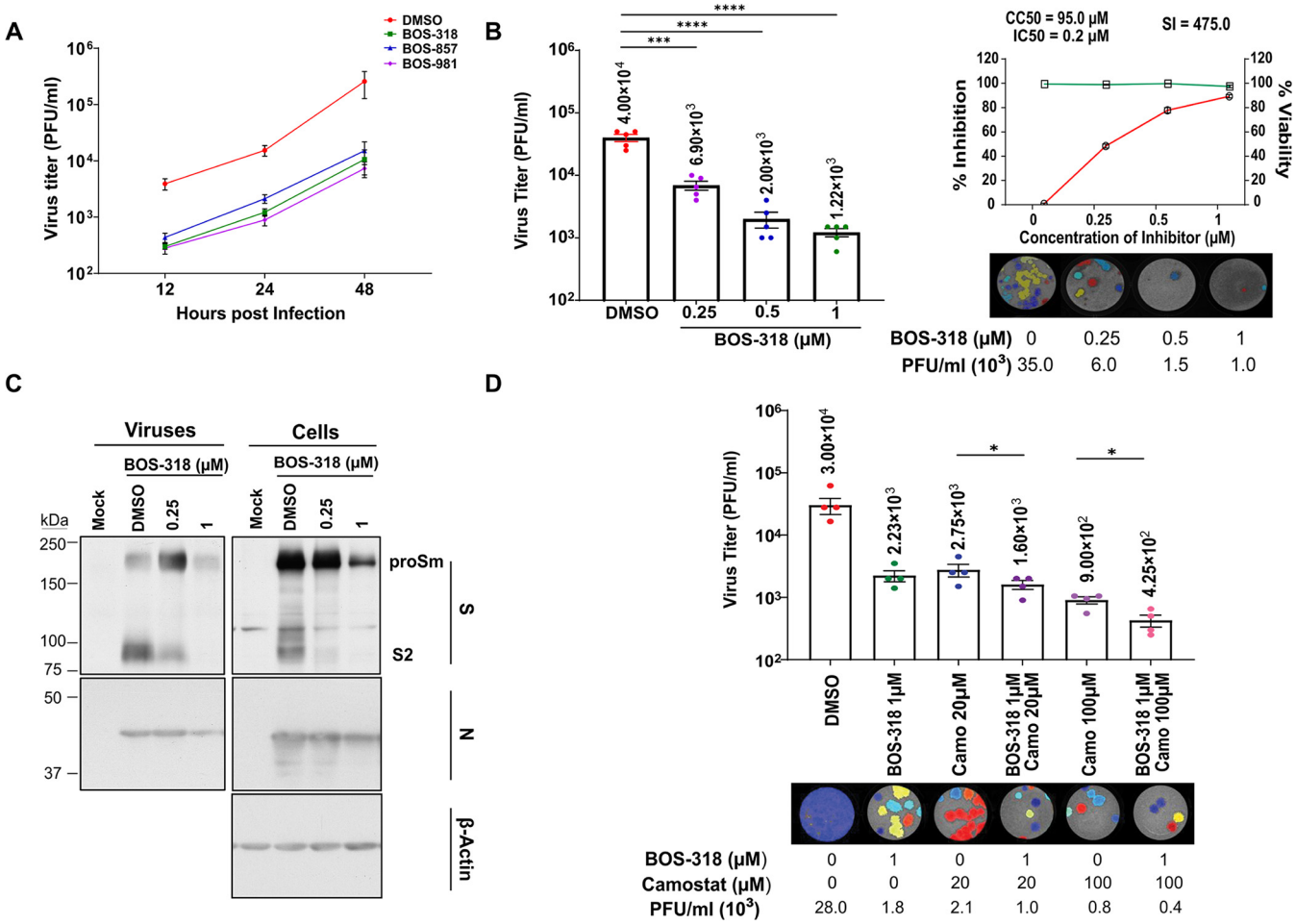

FIG 5 Furin-like inhibitors and camostat treatment decrease SARS-CoV-2 infection in Calu-3 cells. (A) Replication kinetics was studied at 12, 24, and 48 h postinfection by plaque assay to determine PFU of SARS-CoV-2 in the supernatant of infected Calu-3 cells treated or not with 1 μM BOS-318, BOS-857, and BOS-981. A line graph presents results of the triplicate plaque assay results (mean ± SD). (B) Virus titers in the supernatant (24 h postinfection) of infected Calu-3 cells treated with the indicated concentrations of BOS-318 were determined by plaque assay (mean ± SD of triplicates) (left). The selectivity index (SI) of BOS-318 in Calu-3 cells as shown in top right panel was determined by 50% cytotoxic concentration (CC_{50})/half-maximal inhibitory concentration (IC_{50}). The left *y* axis indicates the inhibition of virus titer relative to that of the untreated control group (red). The right *y* axis indicates cell viability relative to that of the untreated control group (green). The CC_{50}, IC_{50}, and SI values for each inhibitor are as shown. Representative analyzed plaque images of infected Calu-3 cells treated with indicated doses of BOS inhibitors are shown at the bottom right. (C) Immunoblots for the infected Calu-3 cells (right) and viral particles secreted in the supernatant (left) with and without treatment with BOS inhibitors indicate reduced viral protein levels. Immunoblots were probed for the full-length ($proS_m$) and cleaved (S2) fragments of viral S protein and nucleocapsid (N) protein as indicated; β-actin was included as the loading control for the cells. (D) Virus titers in the supernatant (24 h postinfection) of infected Calu-3 cells treated with BOS-318 and/or camostat (Camo) were determined by plaque assay (mean ± SD of duplicates) (top). Representative analyzed plaque wells of infected Calu-3 cells are shown. Imaged plaque plates were processed, and plaques were counted using algorithm-based Matlab software as described in Materials and Methods.

HIV particles pseudotyped with WT, μS1/S2, or μS2′ S protein, we observed that the viral entry of μS1/S2-S pseudovirions was ~10-fold reduced in Calu-3 cells (Fig. 8A). In contrast, all three pseudotyped viruses were at least 10-fold more infectious in HEK293T-ACE2 cells, suggesting that S priming at S1/S2 is required for optimal viral entry in Calu-3 cells but dispensable or perhaps even less desirable in HEK293T-ACE2 cells (Fig. 8A). Since these findings were similar to those in Vero E6 cells (43), we surmise that viral entry in HEK293T-ACE2 cells was through the same pH-dependent, endocytic route as reported for Vero cells (44, 45). This agrees with the fact that HEK293 cells allow endocytosis of SARS-CoV-2 pseudovirions via clathrin-coated vesicles (46). In the case of μS2′ S-expressing viral particles, entry was more efficient in both cell types (Fig. 8A, compare the same-colored dots between WT S and μS2′ S in the absence of BOS inhibitors), implying that S cleavage at the S2′-optimized furin-like site could enhance viral entry. When BOS-318 was present during biosynthesis of pseudovirions, processing of WT S and μS2′ S was blocked (Fig. 8B), leading to reductions

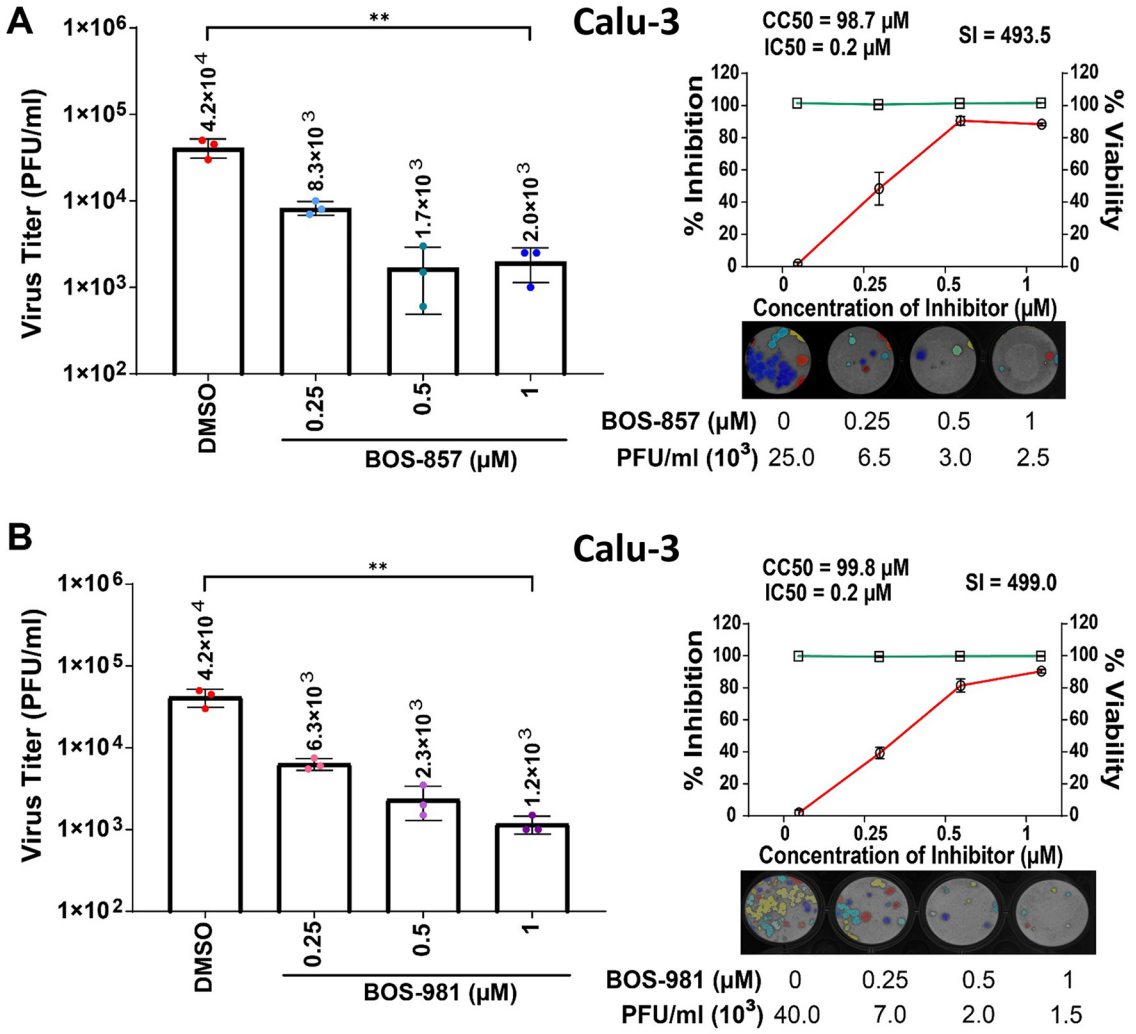

FIG 6 Furin-like inhibitors strongly reduce SARS-CoV-2 infection in Calu-3 cells. Calu-3 cells were treated with indicated concentrations of BOS-857 (A) and BOS-981 (B) and infected with SARS-CoV-2 for 24 h. Virus titers in the supernatant were determined by plaque assay on Vero E6 cells (mean ± SD of triplicates). The selectivity indices of BOS-857 and BOS-981 in Calu-3 cells as shown at the top right were determined by CC_{50}/IC_{50}. The left *y* axis indicates the inhibition of virus titer relative to that of the untreated control group (red). The right *y* axis indicates the cell viability relative to that of the untreated control group (green). Representative analyzed plaque wells of infected Calu-3 cells are shown. Imaged plaque plates were processed, and plaques were counted using algorithm-based Matlab software as described in Materials and Methods.

in viral entry in Calu-3 cells of ~3.6- and ~12.5-fold, respectively (Fig. 8A). Thus, BOS-318 treatment phenocopied the effect of μS1/S2 in both cell types. In addition, BOS-318 treatment enhanced viral entry in HEK293T-ACE2 cells ~10-fold for WT S and ~2-fold for μS2′ S (Fig. 8A), suggesting that viral entry by the pH-dependent pathway does not require furin processing.

Having observed the negative effect of BOS-318 on S processing by particle-producing cells, we asked whether pretreating target cells with BOS-318 would also affect entry of SARS-CoV-2 pseudoparticles. In Calu-3 cells, in which viral entry occurs primarily through fusion at the plasma membrane (44), we observed reduced viral entry by ~3.8-fold for WT S and ~14-fold for μS2′ S (Fig. 8C). This emphasizes a significant contribution of furin to the processing and priming of S at the plasma membrane of Calu-3 cells after ACE2 recognition. The fact that BOS-318 had a more pronounced effect on entry by μS2′ S-containing viral particles was not surprising given the very efficient S2′ processing of this mutant by furin (Fig. 2D). Of note, 100 μM camostat reduced viral entry of WT-S-carrying pseudoparticles ~8.6-fold,

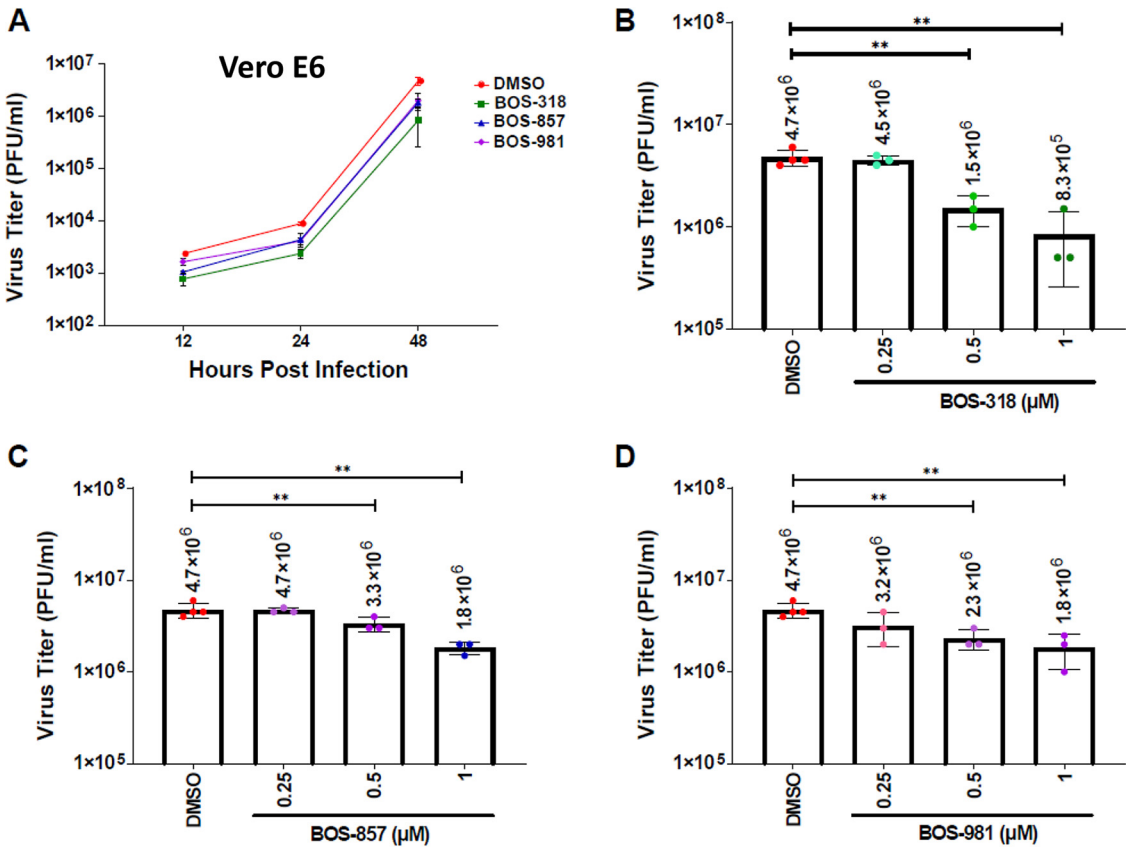

FIG 7 Furin-like inhibitors modestly reduce virus production in SARS-CoV-2-infected Vero E6 cells in a concentration-dependent manner. (A) Vero E6 cells treated or not with 1 μM BOS-318, BOS-857, or BOS-981 were infected with SARS-CoV-2 for up to 45 h. Virus titers in the supernatant obtained at 12, 24, and 48 h postinfection were determined by plaque assay on Vero E6 cells. A line graph presents results of the triplicate plaque assay (mean ± SD). (B to D) Virus released in the supernatant (48 h postinfection) of infected Vero E6 cells treated with indicated concentrations of BOS-318 (B), BOS-857 (C), or BOS-981 (D) were determined by plaque assay (mean ± SD of triplicates).

compared to ~3.2-fold for those carrying μS2′ S (Fig. 8C). This suggests that furin plays a more prominent role in the entry of μS2′ S versus WT S viral particles. Lastly, the combined pretreatment with both BOS-318 and camostat led to a complete block of viral entry, highlighting the synergistic roles of furin and TMPRSS2 in mediating viral fusion at the plasma membrane.

Furin-like inhibitors decrease cell-to-cell fusion and syncytium formation. To assess whether BOS inhibitors also affect cell-to-cell fusion, we developed a coculture assay in which donor HeLa cells express HIV Tat and the fusogenic S protein, while acceptor HeLa TZM-bl cells express ACE2 and Tat-driven luciferase (47) (Fig. 9A). ACE2 expression in TZM-bl (Fig. 9B, panel a [control]) allowed fusion with HeLa-expressing S protein (Fig. 9B, panels b and c), but no fusion was observed with μS1/S2 S (Fig. 9B, panel d). Using this assay, we found that while donor cells expressing WT S led to syncytium formation (Fig. 9B, panels b and c) and a >10-fold increase in cell-to-cell fusion compared to that in control (empty vector [V], no S) cells (Fig. 9C), donor cells expressing μS1/S2 S did not promote any cell-to-cell fusion even in the presence of ACE2 (Fig. 9B panel d, and Fig. 9C and D). Consistent with the latter finding, we observed an almost complete loss of cell fusion when donor cells were treated with BOS inhibitors or the PC inhibitor decanoyl-RVKR-cmk (RVKR; Fig. 9C) (41), emphasizing the critical role of furin cleavage in promoting ACE2-dependent cell-to-cell fusion in the context of acceptor cells lacking endogenous TMPRSS2, such as HeLa cells. This fusion assay also enabled the assessment of the effects of some worldwide-spreading S protein variants of SARS-CoV-2, which affect viral traits such as transmissibility, pathogenicity, host range, and antigenicity of the virus (48, 49). Among these, we selected mutants that modify the Pro at the P5 position of the S1/S2 site (Fig. 1A), i.e., the P681H and P681R

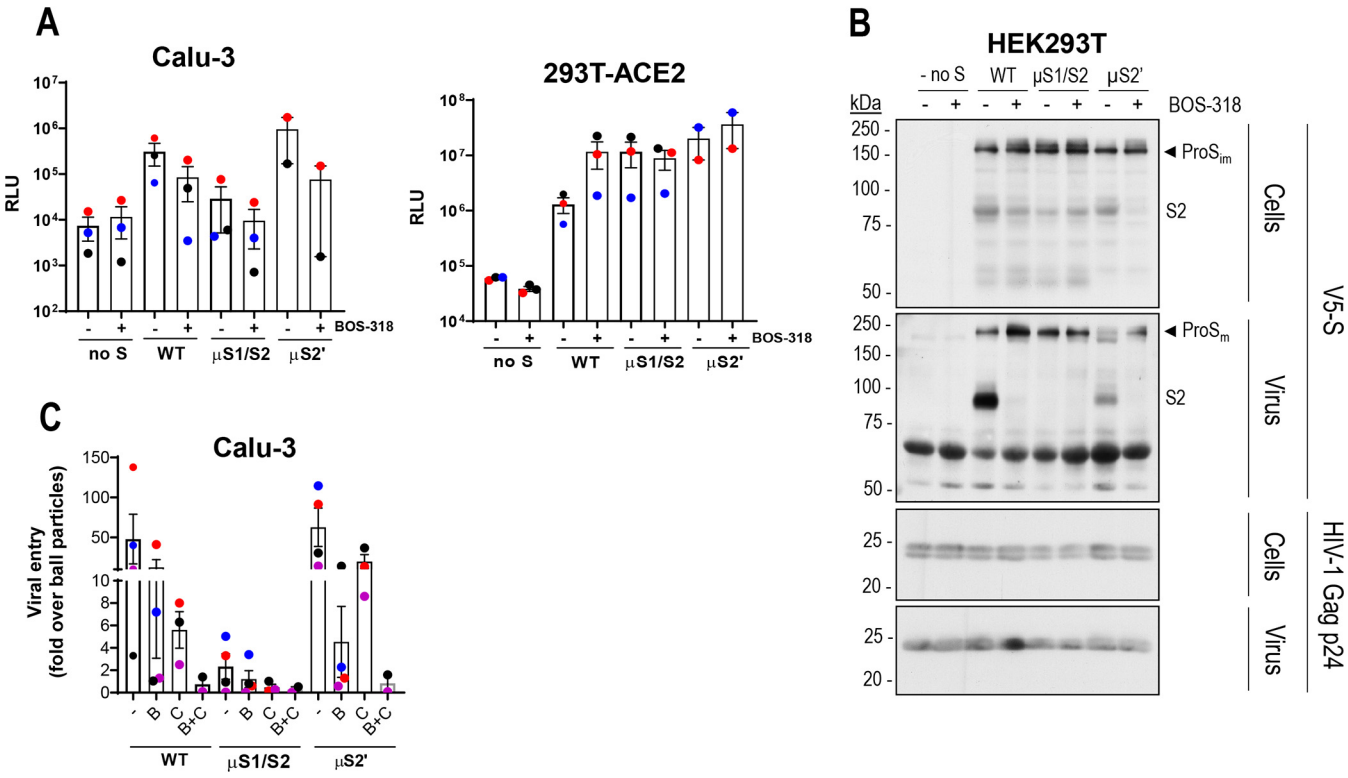

FIG 8 Processing of SARS-CoV-2 S by furin-like convertases and TMPRSS2 is critical for viral entry in human lung epithelial cells but not in model HEK293 cells stably expressing ACE2. (A) Furin cleavage of proS at the S1/S2 site is required for SARS-CoV-2 pseudoviral entry in Calu-3 cells (left) but not HEK293T-ACE2 cells (right). Cells were inoculated with nanoluciferase-expressing HIV particles pseudotyped with SARS-CoV-2: wild-type spike, double Ala mutant spike (μS1/S2), or furin-optimized spike (mS2′). Inhibition of proS processing at S1/S2 by a novel furin-like inhibitor (BOS-318) during pseudovirion packaging prevents viral entry in Calu-3 cells but not in HEK293T-ACE2 cells. (B) Western blot analyses show inhibition by BOS-318 of proS processing at the S1/S2 site. Purified pseudovirions and cellular extracts of producing HEK293T17 cells treated or not with BOS-318 inhibitor were separated on an SDS-PAGE gel and analyzed for HIV-1 p24 and V5-tagged S protein (proS_m or cleaved, S2) as indicated. (C) Pretreatment of Calu-3 cells with 1 mM BOS-318 (B), 100 mM Camostat (C), or both (B and C) markedly reduces viral entry. In panels A and C, Calu-3 cells were transduced with nanoluciferase-expressing HIV particles pseudotyped with SARS-CoV-2 WT, μS1/S2, or mS2′ S for 72 h and analyzed for nanoluciferase expression. Viral entry was expressed as fold increase over that given by bald particles (pseudovirions made in the absence of S). Each dot represents a different experiment with median luciferase activity calculated from three biological replicates. Two to four experiments were performed for each cell type. Error bars indicate SD.

associated with the α and δ variants, respectively (7). Our data showed that while the μS2′ mutant did not affect cell-to-cell fusion, the P681H and P681R mutants significantly enhanced it (~2-fold) (Fig. 9D), in line with the higher transmissibility of the associated α and δ SARS-CoV-2 variants (48, 49) and increased cell-to-cell fusion (50).

TMPRSS2 promotes cell-to-cell fusion in the absence of furin-mediated cleavage at S1/S2. *In vitro*, TMPRSS2 did not efficiently cleave the SARS-CoV-2 S1/S2 and S2′ peptides (Fig. 1C), but in contrast to the case with furin, TMPRSS2 cleavage of Ala mutant peptides RRAA, ARAA, and ARAR mimicking the S1/S2 site was detectable under this condition (Fig. 1C). To assess whether TMPRSS2 promoted cell-to-cell fusion by enhancing S2′ cleavage in the complete absence of S1/S2 priming, we generated a new S derivative lacking all Arg at S1/S2, namely, μAS1/S2 ($AAAA_{685}$) S. Hence, this mutant is different from μS1/S2 (Fig. 2B; ARAA mutant) since it would not be cleaved by TMPRSS2 or furin. Cell-to cell fusion was assessed following incubation of cells expressing WT S or μAS1/S2 S with acceptor cells expressing ACE2 or ACE2 plus TMPRSS2. In this context, TMPRSS2 reduced fusion of WT S ~2.6-fold and enhanced that of μAS1/S2 S ~3.1-fold (Fig. 10A). Camostat completely restored TMPRSS2-reduced fusion with WT S and largely attenuated the TMPRSS2-enhanced fusion with μAS1/S2 (Fig. 10A). The results with μAS1/S2 revealed that in the presence of ACE2, TMPRSS2 could enhance fusion in the absence of S1/S2 priming. We next assessed whether this effect could be related to the differential processing of the S protein and/or to ACE2 receptor

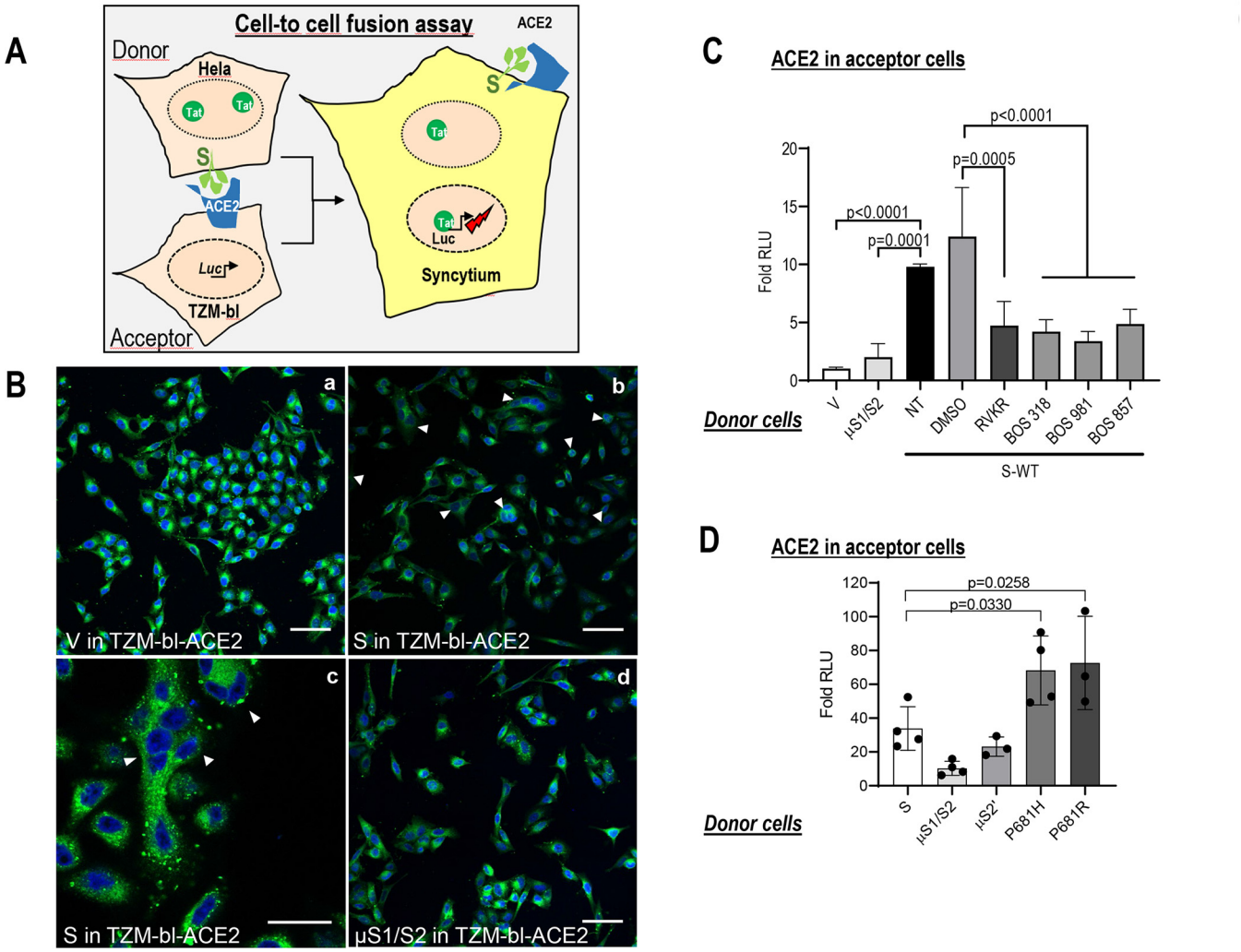

FIG 9 Spike-induced cell-to-cell fusion relies on Furin cleavage at S1/S2. (A) Cell-to-cell fusion between donor cells (HeLa) expressing the fusogenic SARS-CoV-2 spike protein (S) along with the HIV transactivator Tat and acceptor cells (TZM-bl) that express ACE2. Upon fusion, Tat is transferred from donor to acceptor cells, thereby inducing luciferase expression. (B) HeLa cells transfected with an empty vector (a) or expressing SARS-CoV-2 spike (b, seen at higher magnification in panel c), or μS1/S2 (d) were cocultured with TZM-bl cells for 18 h and the number of syncytia (white arrowheads) was examined using CellMask to probe for the plasma membrane and DAPI to stain the nuclei. Cell-to-cell fusion (white arrowheads) was evaluated using confocal microscopy. Scale bars = 60 μm for panels a, b, and d and 30 μm for panel c. (C) Donor cells were transfected with vectors expressing either no protein (empty vector), μS1/S2, or WT spike in the absence (NT) or presence (DMSO) of a vehicle or with the furin inhibitors BOS-318, BOS-981, BOS-857 (300 nM), and RVKR (10 μM). Acceptor cells were transfected with a vector expressing ACE2. After 48 h, donor and acceptor cells were cocultured for 18 h. Relative luminescence units (RLU) were normalized to the V value arbitrarily set to 1. Data are presented as mean values ± SD (n = 3); one-way analysis of variance (ANOVA) and Dunn-Sidàk multiple-comparison test were used. (D) Donor HeLa cells expressing WT S or the indicated S mutants and variants were cocultured with acceptor TZM-bl cells expressing ACE2. The extent of fusion is represented as a ratio between the RLU measured for each condition and that of donor cells expressing empty vector. The bar graph represents the average of 3 experiments performed in triplicates. Data are presented as mean values ± SEM (n = 3). One-way ANOVA and Bonferroni multiple-comparison test and two-way ANOVA and Dunn-Sidàk multiple-comparison test were used.

shedding by TMPRSS2 (51). Western blot (WB) analyses of cell lysates showed that treatment of acceptor cells expressing ACE2 and TMPRSS2 with 120 μM camostat eliminated the enhanced TMPRSS2-induced production of S2′ observed with WT S (Fig. 10B) but not with μAS1/S2 (Fig. 10C), suggesting that the latter S2′ is likely generated by endogenous furin. These data emphasize that TMPRSSS2 cannot process the spike glycoprotein into S2′ in the absence of prior S1/S2 cleavage, even in the presence of ACE2. Notably, the release of S1 derived from WT S in the cell culture media was not affected by the presence of TMPRSS2 (Fig. 10B), suggesting that the secreted S1 primarily results from furin cleavage of WT S at S1/S2. Finally, we observed that TMPRSS2-induced secretion of a longer (~175-kDa) fragment from μAS1/S2, referred to here as $S1_L$, which was not detected in the presence of camostat (Fig. 10C). The molecular weight of $S1_L$

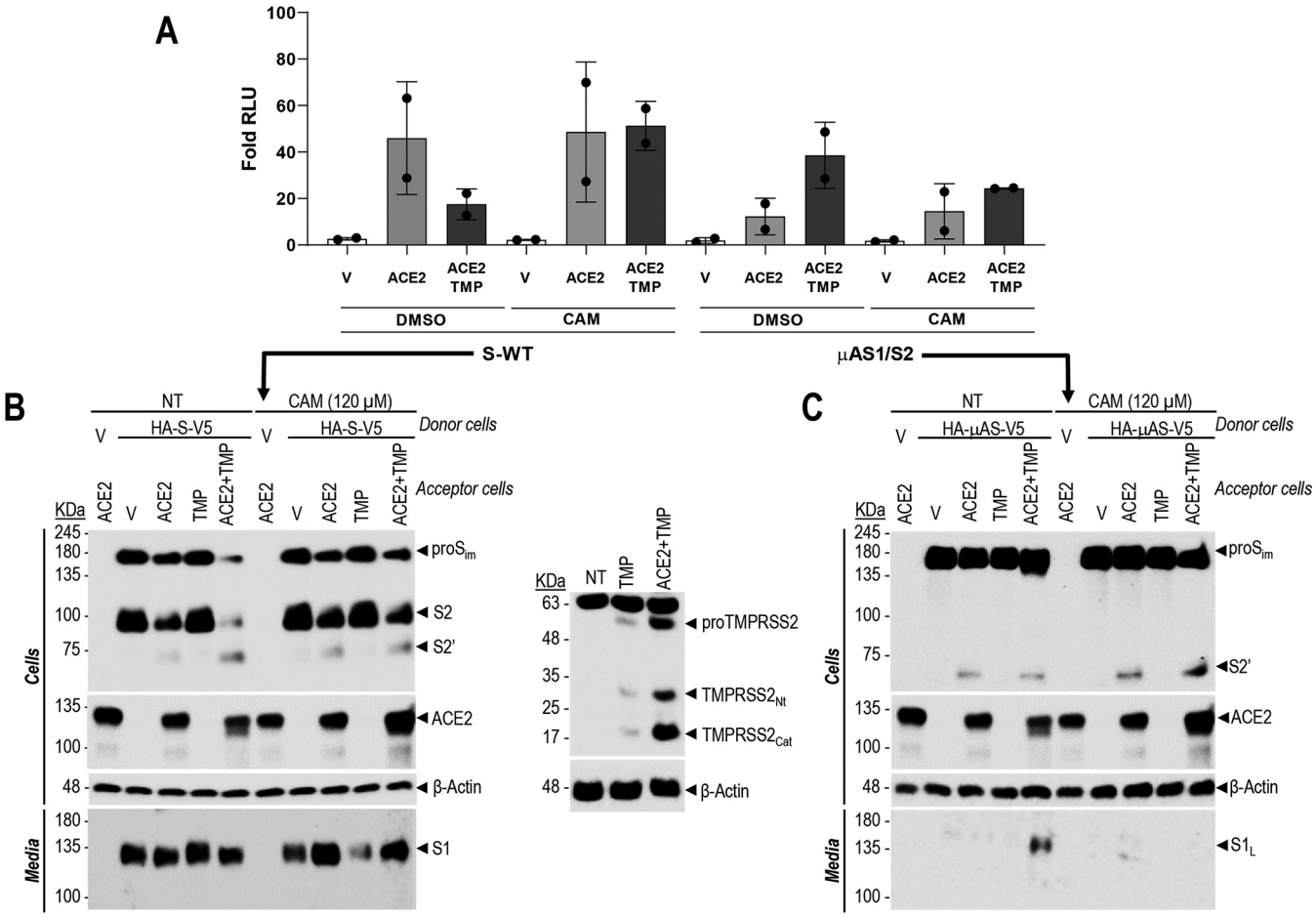

FIG 10 Exogenous TMPRSS2-generated shedding of ACE2 differentially regulates S-induced fusion at the plasma membrane of WT S versus μAS1/S2. Donor HeLa cells expressing doubly tagged (N-terminal HA tag and C-terminal V5 tag) WT spike glycoprotein or its S1/S2 mutant (μAS1/S2) were cocultured with acceptor TZM-bl cells expressing (empty vector), ACE2, or ACE2 plus TMPRSS2 (TMP) and treated with DMSO (vehicle control) or camostat (120 μM). Within the same experiment, cell-to-cell fusion (A) was assessed in parallel with spike processing in cells and media by Western blotting (B and C). (A) The extent of fusion is represented as a ratio between the RLU measured for each condition and that of donor cells expressing V. The bar graph represents the average of 2 experiments performed in triplicates. (B and C). Western blot analyses of media and cell extracts of the cocultured cells with donor cells overexpressing doubly tagged (N-terminal HA tag and C-terminal V5 tag) spike glycoprotein, WT (B) or μAS1/S2 (C). Media were subjected to immunoprecipitation with anti-HA agarose for the secreted forms of spike protein (S1 and $S1_L$), followed by Western blotting with anti HA-HRP. In the cell extracts, spike glycoproteins and ACE2 were immunoblotted with anti-V5 MAb and a polyclonal ACE2 antibody, respectively. The data are representative of those from three independent experiments. The Western blot analyses of TMPRSS2 (using a TMPRSS2 antibody) in the cells are shown separately, emphasizing the migration positions of the zymogen proTMPRSS2 and its autocatalytically generated products: the N-terminal $TMPRSS2_{Nt}$ and C-terminal catalytic $TMPRSS2_{Cat}$.

indicates that it results from a direct cleavage of μAS1/S2 S at S2′ (Fig. 10B). Together, our data indicate that TMPRSS2 can enhance cell-to-cell fusion when S priming is blocked by facilitating the release of $S1_L$ after S2′ cleavage.

Our next goal was to further decipher the contribution of ACE2 cleavage by TMPRSS2 and the seemingly opposite effects of TMPRSS2 on fusion activity with WT S and μAS1/S2 S (Fig. 10A). Since TMPRSS2 cleaves at single Arg and Lys residues (52), we tested the effect of multiple Arg/Lys-to-Ala mutations in segments close to the transmembrane domain of ACE2 (C0+C4 in Fig. 11A), which were previously proposed to limit TMPRSS2-induced shedding (51). Accordingly, WB analyses (Fig. 11B) revealed that TMPRSS2, but not its active-site Ser mutant S441A (μTMPRSS2 [Fig. 11B and E]), shed the membrane-bound ~120-kDa WT ACE2, releasing a major ~95-kDa and a minor ~80-kDa form into the medium (sACE2). In contrast, TMPRSS2 primarily generated the ~80-kDa fragment from the ACE2 C0+C4 mutant. It should be mentioned that in the absence of TMPRSS2, the extents of fusion for both WT S and μAS1/S2 S were comparable between WT ACE2 and the ACE2 C0+C4. Interestingly, in the context of the ACE2 C0+C4 receptor mutant

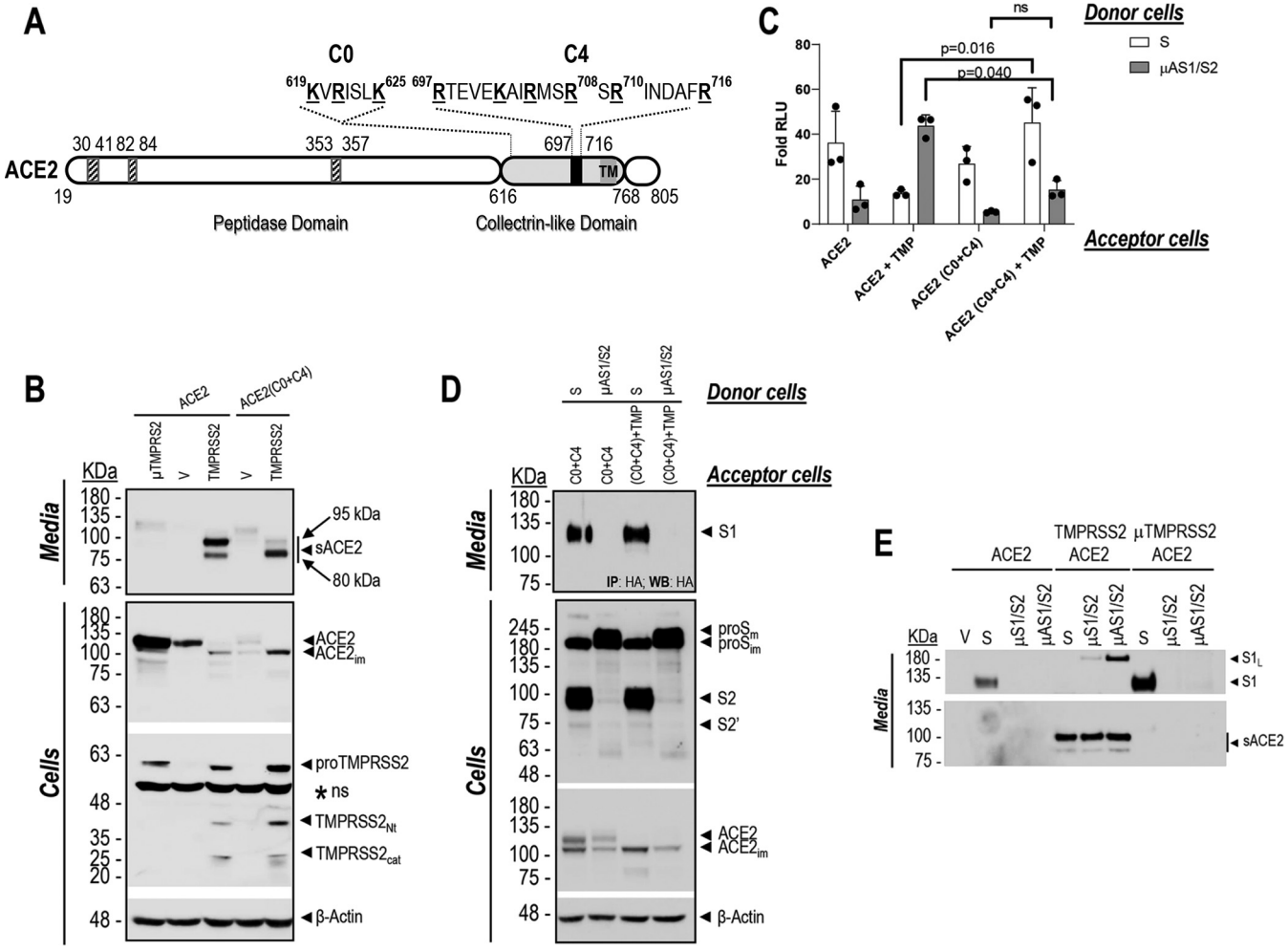

FIG 11 The C-terminal collectrin-like domain of ACE2 may be critical for the regulation of cell-to-cell fusion of spike glycoprotein when exogenous TMPRSS2 is present: effect on secretion of $S1_L$. (A) Schematic representation of the primary structure of human ACE2 with emphasis on the C-terminal collectrin-like domain (aa 616 to 768 [light gray]), TMPRSS2 cleavage region (aa 697 to 716 [black]), and the polybasic amino acid segments in which K/R were mutated to A (C0 and C4) (amino acids underlined and in bold). Also shown are the peptidase domain (aa 19 to 615 [white]) containing the regions involved in the interaction with the spike SARS-CoV protein (hatched) and transmembrane domain (TM). (B) HeLa cells were cotransfected with ACE2 (WT ACE2 or the ACE2 C0+C4 mutant) and TMPRSS2 (WT or the S441A active-site mutant [μTMPRSS2]) or empty vector. Media and cell extracts were analyzed by Western blotting for shed ACE2 (sACE2) and ACE2, respectively. The migration positions of the ~95-kDa and ~80-kDa sACE2 in the media, as well as the intracellular disulfide bridged catalytic (cat) and N-terminal (Nt) fragments of TMPRSS2, are emphasized. (C) Donor HeLa cells expressing WT S-HA or μAS1/S2-HA were cocultured with acceptor TZM-bl cells expressing ACE2, WT ACE2, or the ACE2 C0+C4 mutant in presence or absence of TMPRSS2. From the same experiment, cell-to-cell fusion was assessed (C), in parallel with WB analyses of cells and media (D). The extent of fusion is represented as a ratio between the RLU measured for each condition and that of donor cells expressing an empty vector. The bar graph presents the average of 3 experiments performed in triplicates. Data are presented as mean values ± SD (n = 3). One-way ANOVA and Tukey's multiple-comparison test were performed. (D) Coculture media were subjected to immunoprecipitation with anti-HA agarose for the secreted forms of spike protein (S1) followed by Western blotting with anti-HA-HRP. Spike glycoproteins in the cell extracts were immunoblotted with anti-V5 MAb. The Western blot data are representative of those from three independent experiments. (E) HeLa cells were transiently coexpressed with doubly tagged spike protein (N-terminal HA tag and C-terminal V5 tag), WT S or its mutants, μS1/S2 or μAS1/S2, and ACE2 alone or in combination with WT TMPRSS2 (TMPRSS2) or its S441A active-site mutant (μTMPRSS2), at an S/ACE2/TMPRSS2 ratio of 1:0.5:0.5. The immunoblot of the 24-h-conditioned media was first probed for secreted S1 and $S1_L$ (HA-HRP antibody), stripped, and next probed for sACE2.

and different from the case with WT ACE2 (Fig. 10A and 11C), TMPRSS2 no longer modulated the fusion of both WT S and μAS1/S2 S (Fig. 11C). Importantly, TMPRSS2 did not reduce the levels of S2 when the ACE2 C0+C4 mutant was used (Fig. 11D) as observed with WT ACE2 (Fig. 10B), nor did it reduce fusion (Fig. 11C). Additionally, the TMPRSS2-enhanced secretion of the ~175-kDa $S1_L$ fragment in the absence of S1/S2 cleavage (Fig. 10C and 11E) was no longer detected in the medium when the ACE2 C0+C4 mutant was expressed in acceptor cells (Fig. 11D) and correlated with the lack of fusion of μAS1/S2 S (Fig. 11C). Together, these results suggest that the shedding of an ~95-kDa form of

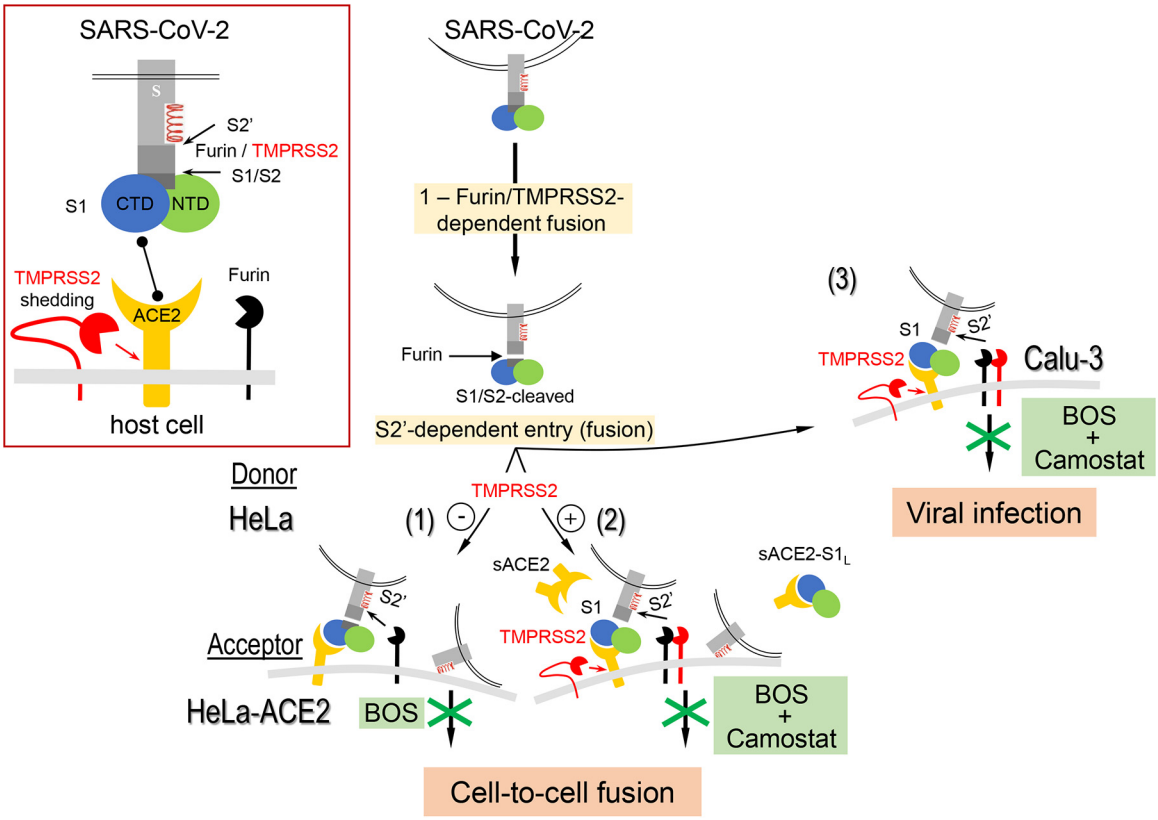

FIG 12 Proposed model for the processing of S protein and its blockade by Furin and TMPRSS2 inhibitors. (Boxed panel) Schematic representation of the S glycoprotein domains of SARS-CoV-2, including the N-terminal (NTD) and C-terminal (CTD) domains of S1, the furin-S1/S2, and the furin/TMPRSS2-S2′ processing sites, as well as the fusogenic α-helix that follows S2. Binding of the receptor binding domain of S1 to the membrane-associated ACE2 in target cells and the cell surface expression of TMPRSS2 and furin are also schematized. (Right portions) (1) BOS inhibitors (or mS1/S2 mutant) completely prevent fusion of donor HeLa cells expressing S glycoprotein with acceptor HeLa-ACE2 cells, which lack endogenous TMPRSS2. In this context, furin is a major processing enzyme cleaving at S1/S2 and generating S2′. (2) In acceptor HeLa cells expressing TMPRSS2 (+), maximal prevention of cell-to-cell fusion can be achieved by a combination of furin (BOS, phenocopying the mS1/S2 or mAS1/S2 mutants) and TMPRSS2 (camostat) inhibitors, which blocks S2′ production, ACE2 shedding (sACE2), and separation of sACE2-S1L complex from S2. (3) Optimal blockade of SARS-CoV-2 infection of Calu-3 cells, which express endogenously both furin and TMPRSS2, is also achieved by a combination of furin (BOS) and TMPRSS2 (camostat) inhibitors.

ACE2 by TMPRSS2 (generated from WT ACE2 but not from the ACE2 C0+C4 mutant) could differently modulate SARS-CoV-2 fusion depending on the efficiency of priming at S1/S2. For the first time, we show that in the absence of furin-mediated priming of S, TMPRSS2 promotes the secretion of a shed form of ACE2 (sACE2) that favors cell-to-cell fusion, likely by binding to the N-terminally extended $S1_L$ (amino acids [aa] 14 to 815) (53) and favoring its release.

DISCUSSION

Furin and TMPRSS2 were both proposed to process the SARS-CoV-2 spike protein and promote viral entry and infection. Here, we functionally characterize the roles of furin and TMPRSS2 and reveal their complementary contributions to SARS-CoV-2 entry and infection. Thus, we show for the first time that three orally active small-molecule nonpeptide furin inhibitors can block viral entry *via* the pH-independent cell surface fusion pathway and that this effect is highly enhanced by a combination of furin and TMPRSS2 inhibitors (Fig. 12). Our data also clearly emphasize the critical importance of ACE2 in the generation of S2′ by both furin and TMPRSS2, which we unambiguously characterized by proteomics to occur at KPS$\underline{KR}_{815}\downarrow$SF. Finally, we demonstrate that shedding of ACE2 into sACE2 by TMPRSS2 likely represents a mechanism by which the virus escapes the effect of furin inhibitors. We suggest that in the absence of S1/S2

priming, sACE2 may facilitate S2′ cleavage and/or release of $S1_L$ and thereby induce the exposure of the C-terminal fusogenic domain and favor viral infection (Fig. 12).

Consistent with previous data (19, 29, 44, 54), processing at S1/S2 is required for optimal viral entry in Calu-3 lung epithelial cells. Indeed, mutation of the arginines in the FCS or blocking S1/S2 cleavage by a series of novel furin inhibitors effectively reduced SARS-CoV-2 entry in Calu-3 cells. In the context of cell-to-cell fusion, mutations of the FCS impaired syncytium formation in HeLa cells in the absence of TMPRSS2 in acceptor cells, and furin inhibitors phenocopied the effect of these S1/S2 mutations. These results highlight the importance of furin in promoting S-mediated cell-to-cell fusion. The facts that furin cleavage at S1/S2 is conserved in SARS-CoV-2 isolated from COVID-19 patients and that ΔPRRA viruses lacking the FCS are poorly infectious in hamsters (55) suggest that blocking viral entry through the pH-independent pathway is a viable approach toward thwarting SARS-CoV-2 dissemination. In this context, the present nontoxic BOS inhibitors deserve consideration as potential antivirals against acute SARS-CoV-2 infection. As observed in adult animal models, short-term inhibition of furin would not cause severe side effects, despite the many physiological functions of this enzyme (21).

Our results demonstrate that furin can process S at S1/S2 and S2′ ($\underline{\mathbf{KR}}_{815}\downarrow$SF) and that the latter cleavage is optimized in the μS2′ variant ($KRRKR_{815}\downarrow$SF), yielding a protein fully competent for fusion in pseudotyping experiments. Importantly, we show that S2′ processing is strongly increased when the ACE2 receptor is expressed. The data suggest that recognition of the ACE2 receptor by the spike protein induces a conformational change of the S2 domain and enhances cleavage of S2′ site by cellular proteases such as furin.

In contrast, TMPRSS2 appears to less efficiently cleave synthetic peptides encompassing the S1/S2 and S2′ cleavage sites than furin (Fig. 1C). TMPRSS2 has been reported to enhance the infectivity of SARS-CoV-1 and MERS-CoV via cleavages of the S protein (52, 56), as reviewed in references 2, 16, and 24. The S1/S2 site $VSLL\underline{R}_{667}\downarrow ST$ of SARS-CoV-1 contains an Arg↓Ser cleavage motif that is propitious to cleavage by TMPRSS2 (52) but not by furin. However, S1 production was minimal and fusion was observed only when donor cells expressing S protein were cocultured with acceptor cells expressing ACE2 and TMPRSS2 (52). In contrast, coculture of HeLa cells expressing SARS-CoV-2 WT S revealed that while the relative levels of soluble S1 fragment were not affected by the presence of TMPRSS2, the latter enhances S2′ levels (Fig. 10B). Since this was not associated with increased cell-to-cell fusion (Fig. 10A), we assert that TMPRSS2 could also modulate cell-to-cell fusion via shedding of ACE2. In the presence of TMPRSS2, the extent of fusion would depend on a combination of S2′ generation, reduced levels of full-length ACE2 receptor (due to shedding), and increased levels of sACE2 that could act as a decoy to inhibit fusion (57). In that context, a human recombinant sACE2 that includes the collectrin domain but lacks the TM domain (hrsACE2, aa 1 to 740) (Fig. 11A) effectively blocked SARS-CoV-2 infection of Vero E6 cells (53). Indeed, our cell-to-cell fusion assay revealed that the ~95-kDa sACE2 primarily produced by TMPRSS2 cleavage of ACE2 resulted in lower levels of ACE2 (Fig. 11B) and impaired WT-S-induced fusion (Fig. 11C). In contrast, the ACE2 C0+C4 mutant was no longer sensitive to TMPRSS2 shedding, suggesting that the ~80-kDa sACE2, likely generated by cleavage upstream of Lys_{619}, may no longer be able to inhibit WT S fusion (Fig. 11C) but may still bind S1, as shown by cryo-electron microscopy (cryo-EM) studies that used a short ACE2 ectodomain (aa 19 to 615) (38). Together, these results suggest that the C-terminal collectrin-like domain (58, 59) of ACE2 (aa 616 to 768) (Fig. 11A), which is lost in the ~80-kDa form, may be critical for sACE2 to inhibit cell-to-cell fusion of WT S. Since Arg_{710} and Arg_{716} within the collectrin-like domain (Fig. 11A) have been implicated in ACE2 dimerization (59), the Ala substitutions in the ACE2 C0+C4 mutant should significantly impair this process. Whether dimerization of ACE2 and the ~95-kDa sACE2 (Fig. 11B) are needed for efficient inhibition of WT-S-induced fusion (57) is yet to be confirmed.

In the context of endogenous expression of ACE2 and TMPRSS2, e.g., in Calu-3 cells (60, 61), our data show that camostat significantly reduced SARS-CoV-2 infectivity (Fig. 5D) and pseudovirus entry (Fig. 8C), revealing that an endogenous, relatively low level TMPRSS2-like activity in Calu-3 cells favors viral entry. Similarly, in the presence of BOS inhibitors or absence of furin cleavage at S1/S2 (μAS1/S2), TMPRSS2 enhances cell-to-cell fusion (Fig. 10A). However, when S1/S2 cleavage occurred, cell-to-cell fusion was reduced by TMPRRS2, a process that, in turn, was blocked by camostat. This suggests that the relative contribution of TMPRSS2 to the shedding of ACE2 into sACE2 and cleavage of S protein at S2′ is cell type dependent or that the mechanism of fusion in the context of viral particle fusion is less sensitive to the decoy effect of sACE2 released by TMPRSS2. Future experiments may unravel the underlying mechanism that would explain the difference between cell-to-cell fusion in HeLa cells expressing relatively high levels of TMPRSS2, versus infection in Calu-3 cells, expressing modest levels of TMPRSS2. However, using cell-to-cell fusion, our study highlights a complex dynamic between S protein, ACE2, furin, and TMPRSS2 and points to a potential role of TMPRSS2, which in the absence of S1/S2 processing (e.g., μAS1/S2 or in the presence of BOS inhibitors) can facilitate cell-to-cell fusion by shedding ACE2 (Fig. 12).

The human airway epithelium is an important site of early SARS-CoV-2 infection (19, 30, 62). The virus can then disseminate to other tissues/cells, such as gut, liver, endothelial cells, and macrophages, where ACE2, furin, and TMPRSS2 are coexpressed (63). While furin is mostly found in the TGN, it is also present in endosomes and on apical/basolateral plasma membranes in polarized cells such as those of the lung, small intestine, and kidney (64). In contrast, TMPRSS2 is mostly found at the apical membrane of secretory epithelia (65), suggesting that both enzymes would be poised to process the S protein on the apical side. Their relative abundance may be an important factor governing which of the two might cleave S at the S2′ cleavage site. The complementarity and interchangeability of these different proteases, together with those in endosomes, likely allow for SARS-CoV-2 to exhibit a wider tropism than SARS-CoV-1 (66). In this context, we note that randomized placebo-controlled clinical trials using the orally administered TMPRSS2 inhibitor camostat mesylate three times a day did not ameliorate COVID-19 symptoms (67), implying that blocking both TMPRSS2 and furin functions could be beneficial, since our results showed that TMPRSS2 activity is preponderant in the absence of S1/S2 cleavage. Furthermore, the intranasal delivery of both agents would be expected to have less severe side effects and be more effective, as it would directly target the airway epithelia of the nose and the lungs, the major sites of SARS-CoV-2 entry.

Together, our results strongly support the notion that a combination of BOS and selective TMPRSS2 inhibitors would provide a more effective blockade against SARS-CoV-2 infection (Fig. 5D and 8C). It would now be interesting to validate *in vivo* whether a combination of a BOS inhibitor and a more potent/selective TMPRSS2 inhibitor (68) together with hydroxychloroquine (44, 69) would synergize the antiviral effect of these entry inhibitors.

The availability for worldwide distribution of various SARS-CoV-2 vaccines represents a major advance to limit the spread of SARS-CoV-2 infections. However, whether they will be effective in patients with impaired immune systems and confer persistent protection against new variants of SARS-CoV-2 is still an open question. If the protective effect of the vaccination remains incomplete, effective antiviral drugs are still needed and could help with early diagnosis of the disease. Ultimately, in case of new emerging coronavirus pandemics (70), the availability of such treatments would constitute a powerful antiviral arsenal to be used in pandemic preparedness.

MATERIALS AND METHODS

Enzymatic PC inhibition by BOS inhibitors. (i) Biochemical assay. The proprotein convertases furin (108-574-Tev-Flag-6×His), PC5A (PCSK5; 115-63-Tev-Flag-6×His), PACE4 (PCSK6; 150-693-Tev-Flag-6×His), and PC7 (PCSK7; 142-634-Tev-Flag-6×His) were purified from BacMam-transduced CHO cells. Reactions were performed in black 384-well polystyrene low-volume plates (Greiner) at a final volume of

10 μL. BOS inhibitors (BOS-318, BOS-857, and BOS-981) were dissolved in dimethyl sulfoxide (DMSO; 1 mM) and serially diluted 1 to 3 with DMSO through 11 dilutions to provide a final compound concentration range from 0.00017 to 10 μM. A 0.05-μL volume of each concentration was transferred to the corresponding well of an assay plate, and then 5 μL of furin, PCSK5, PCSK6, and PCSK7 in assay buffer (100 mM HEPES [pH 7.5], 1 mM $CaCl_2$, and 0.005% Triton X-100) was added using a Multidrop Combi dispenser (Thermo) to the compound plates to give final protein concentrations of 0.02, 0.5, 2.5, and 1.0 nM, respectively. The plates were mixed by inversion, and following a 30-min preincubation of enzyme with compound at room temperature (~22°C), the substrate FAM-QRVRRAVGIDK-TAMRA (AnaSpec; no. 808143; 5 μL of a 1, 0.25, 0.20, and 0.5 μM solution in assay buffer for furin, PCSK5, PCSK6, and PCSK7, respectively) was added using a Multidrop Combi dispenser. The plates were centrifuged at 500 $\times$ *g* for 1 min and incubated at room temperature for 2 h. Enzyme inhibition was then quantified using an Envision instrument (PerkinElmer). Data were normalized to maximal inhibition determined by 1 μM decanoyl-Arg-Val-Lys-Arg-chloromethylketone (Calbiochem; no. 344930).

(ii) Golgi imaging assay. The Golgi imaging assay uses an image-based platform to evaluate the intracellular activity of furin inhibitors. Reactions were performed in black 384-well, tissue culture-treated, clear-bottom plates (Greiner). Compounds dissolved in DMSO (1.0 mM) were serially 3-fold diluted to give a final compound concentration range from 0.00017 to 10 μM. Analyses were initiated by the addition of U2OS cells simultaneously transduced with a BacMam-delivered construct containing a Golgi-targeting sequence followed by a 12-amino-acid furin/PCSK cleavage site from bone morphogenic protein 10 (BMP10) and then green fluorescent protein (GFP) at the C terminus. The dibasic furin cleavage site sequence was flanked by glycine-rich linkers (GalNAc-T2-GGGGS-DSTARIRRNAKG-GGGGS-GFP). Briefly, frozen cells are thawed in assay medium (Dulbecco's modified Eagle's medium [DMEM] nutritional mixture F-12 [Ham] without phenol red containing 5% fetal bovine serum [FBS]) and diluted to deliver 6,000 cells/well (50 μL) to the plate using a Multidrop Combi dispenser (Thermo). After a 24-h incubation period at 37°C, the cells are stained with CellMask deep red stain and fixed in paraformaldehyde, and the nuclei were stained using Hoechst 33342. The Golgi-targeted GFP forms bright punctate clusters within the cell. In the absence of a furin/PCSK inhibitor, the endogenous protease cleaves GFP from its *N*-acetylgalactosaminyltransferase 2 Golgi tether, releasing GFP into the Golgi lumen, where fluorescence was diluted below the threshold of assay sensitivity. In the presence of a cell-permeative furin/PCSK inhibitor, GFP fluorescence increased as intra-Golgi protease activity was reduced. Cellular GFP intensity was determined by image-based acquisition (Incell 2200; PerkinElmer) at a magnification of $\times$40 with 4 fields measured per well. Multiscale top hat segmentation was used to identify the GFP-tagged puncta and to quantitate the average fluorescence of all puncta on a per-cell basis. Cellular toxicity was determined in parallel.

(iii) Furin and TMPRSS2 fluorogenic assays. Recombinant furin was purchased from BioLegend (no. 719406), human recombinant TRMPSS2 from CliniSciences (reference no. LS-G57269-100), and the DABCYL/Glu-EDANS labeled peptides encompassing the different cleavage sites (Table 1) were purchased from Genscript. Reactions were performed at room temperature in black 384-well polystyrene low-volume plates (CELLSTAR-Greiner Bio-One; 784476) at a final volume of 15 μL. The fluorescent peptides were used at 5 μM and the reactions were performed in 50 mM Tris buffer (pH 6.5 or 7.5), 0.2% Triton X-100, 1 mM $CaCl_2$; furin was added at a final concentration of 0.2 to 100 nM. BOS inhibitors (BOS-318, BOS-857, and BOS-981) were dissolved in DMSO (1 mM) and serially diluted 1 to 2 with DMSO to provide a final compound concentration range from 50 μM to 0.01 nM with 5% DMSO in the enzymatic assay. For TMPRSS2, the fluorescent peptides were used at 5 μM and the reactions were performed in 50 mM Tris buffer (pH 8) and 150 mM NaCl, and TMPRSS2 was added at a final concentration of 50 nM. Cleavage of the synthetic peptides was quantitated by determining the increase of EDANS (493 nm) fluorescence following release of the DABCYL quencher, which was excited at 335 nm using a Safire 2 Tecan fluorimeter. The fluorescence was followed for 90 min, and the enzymatic activity was deduced by measurement of the increase of fluorescence during the linear phase of the reaction. Each reaction was performed in triplicate, and the standard deviation was calculated using Excel-ecart type function:

$$\sqrt{\frac{\sum (x-\bar{x})^2}{(n-1)}}$$

Plasmids. Singly tagged (C-terminal V5 tag) or doubly tagged (N-terminal hemagglutinin [HA] tag and C-terminal V5 tag) spike glycoprotein of SARS-CoV-2 (optimized sequence) and its mutants were cloned into the pIRES2-EGFP vector. Site-directed mutagenesis was achieved using a QuikChange kit (Stratagene, CA) according to the manufacturer's instructions. Plasmid pCI-NEO-hACE2 was received from D. W. Lambert (University of Leeds), and plasmid pIRES-NEO3-hTMPRSS2 was received from P. Jolicoeur (IRCM). The ΔEnv Vpr luciferase reporter vector (pNL4-3.Luc.R-E-) was obtained from Nathaniel Landau through the NIH AIDS Reagent Program, whereas the pHIV-1NL4-3 ΔEnv-NanoLuc construct was a kind gift from Paul Bieniasz. Plasmids encoding vesicular stomatitis virus glycoprotein (VSV-G), as well as HIV-1 Env and Tat, were previously described (71, 72).

Cell culture and transfection. Monolayers of HeLa, HEK293T, HEK293T17, Vero E6, and Calu-3 cells were cultured in 5% CO_2 at 37°C in DMEM (Wisent) supplemented with 10% (vol/vol) FBS (Wisent). HEK293T-ACE2 cells (73), a generous gift from Paul Bieniasz, were maintained in DMEM containing 10% FBS, 1% nonessential amino acids (NEAA) and 50 μg/mL of blasticidin (InvivoGen). The cells were transfected with JetPrime transfection reagent according to the manufacturer's instructions (Polyplus-transfection, New York, NY). At 24 h posttransfection, the culture media were changed to serum free and cells

incubated for an additional 24 h. To establish the HeLa cells stably expressing human ACE2, transfected cells were selected using media containing 500 μg/mL of neomycin (G418; Wisent).

For knockdown of furin in HeLa cells, an optimized set of 4 small interfering RNAs (siRNAs; SMARTPool) targeted against human furin were purchased from Horizon Discoveries (PerkinElmer, Lafayette, LA) and transfections of HeLa cells were carried out using INTERFERin (Polyplus-transfection) as recommended by the manufacturer.

To generate HIV particles pseudotyped with SARS-CoV-2 S, HEK293T17 cells (600,000 cells plated in a 6-well vessel) were transfected with 1 μg of pNL4-3.Luc.R-E- (or pHIV-1NLΔEnv-NanoLuc) in the presence or absence of 0.3 μg of pIR-2019-nCoV-S V5 plasmids using Lipofectamine 3000 (Life Technologies). In certain experiments, HEK293T17 cells were treated with BOS inhibitors at 6 h posttransfection. Pseudovirions expressing the nanoluciferase or firefly luciferase were collected at 24 h or 48 h posttransfection, respectively. Viral supernatants were clarified by centrifugation at 300 $\times$ *g* and passed through a 0.45-μm-pore-size polyvinylidene fluoride (PVDF; Millipore) syringe filter (Millipore; SLGVR33RS), and aliquots were frozen at −80°C. For WB analysis of purified pseudovirions, viral supernatants were concentrated by ultracentrifugation on a 20% sucrose cushion for 3 h at 35,000 rpm (Beckman Coulter OPTIMA XE; Ti70.1 rotor). HIV particles lacking the SARS-CoV-2 S glycoprotein served as a negative control in all experiments.

Cell viability assay using MTT. Cells, seeded in a 96-well plate the day before at 10,000 (HEK-293T and Vero E6) or 50,000 (Calu-3), were treated with serial 10-fold dilutions of BOS inhibitors for up to 48 h. Cells treated with a vehicle alone were used as a negative control. 3-(4,5-Dimethyl-2-thiazolyl)-2,5-diphenyl-2H-tetrazolium bromide (MTT) was subsequently added to the medium (final concentration, 2.5 mg/mL), and cells were further incubated for 4 h at 37°C. After removal of the culture media, DMSO was added and absorbance was read at 595 nm using a microplate spectrophotometer. The data from two independent experiments done in triplicates were used to calculate the 50% cytotoxic concentration (CC_{50}) by nonlinear regression using GraphPad Prism v5.0 software.

qPCR analyses. RNA from transfected HeLa cells were extracted using TRIzol, as recommended by the manufacturer (Invitrogen, Burlington, ON, Canada). cDNA synthesis and quantitative reverse transcription-PCR (qPCR) were performed as previously described (74). Primers from neighboring exons were used to measure PC5, furin, PC7, PACE4, and human TATA box binding protein (TBP) expression. The sense and antisense oligonucleotides used for qPCR of the PCs and TBP were as follows: PC5, 5′-ACTCTTCAGAGGGTGGCTA and 5′-GCTGGAACAGTTCTTGAATC; furin, 5′-CATGACTACTCTGCTGATGG and 5′-GAACGAGAGTGAACTTGGTC; PACE4, 5′-CGGGAACCAAGTCTCAACTTCT and 5′-CAGTTTGTAA ACCCTTCATTGGAA; PC7, 5′-ACACCATCCAGGACATTGCA and 5′-GGGTCATTAGAGTTGAGGTCATAGC; and TBP, 5′-CGAATATAATCCCAAGCGGTTT and 5′-GTGGTTCGTGGCTCTCTTATCC.

Western blots. The cells were washed with phosphate-buffered saline (PBS) and then lysed using radioimmunoprecipitation assay (RIPA) buffer (1% Triton X-100, 150 mM NaCl, 5 mM EDTA, and 50 mM Tris [pH 7.5]) for 30 min at 4°C. The cell lysates were collected after centrifugation at 14,000 $\times$ *g* for 10 min. The proteins were separated on 7% Tris-glycine or 8% Tricine gels by SDS-PAGE and transferred to a PVDF membrane (PerkinElmer). The proteins were revealed using a V5 monoclonal antibody (MAb) (V2660; 1:5,000; Invitrogen), ACE2 antibody (rabbit monoclonal antibody ab108252; 1:3,000; Abcam), actin antibody (rabbit polyclonal A2066; 1:5,000; Sigma), TMPRSS2 antibody (rabbit monoclonal antibody ab92323; 1:1,000; Abcam), or HA-horseradish peroxidase (HRP) antibody (12-013-819; 1:3,500; Roche). The antigen-antibody complexes were visualized using appropriate HRP-conjugated secondary antibodies and an enhanced chemiluminescence kit (ECL; Amersham or Bio-Rad), and normalization to β-actin was reported. Quantification of immunoreactive proteins was performed using Image Lab software (Bio-Rad).

For analysis of SARS-CoV-2 S virions or pseudovirions, protein extracts of purified viral particles and corresponding producing cells (Calu-3 or 293T17, respectively) were resolved on 10% Tris-glycine gels and immunoblotted for spike, nucleocapsid, HIV-1 Gag p24, or actin using anti-V5 (for pseudovirion detection; V2660)/anti-S2 (for virion detection; Sino Biologicals; 40590-T62), anti-N (Sino Biologicals; 40143-MM05), anti-p24 (Maine Biotechnology Services (MBS) hybridoma line 31-90-25), or anti-actin (MP Biomedicals; SKU 08691001), respectively.

Glycosidase treatment. Proteins (30 to 50 μg) were digested for 90 min at 37°C with endoglycosidase H (endo-H; P0702L) or endoglycosidase F (endo-F; P0705S) as recommended by the manufacturer (New England BioLabs).

Inhibitor treatment. At 24 h posttransfection, cells were incubated for 6 h with two pan-PC inhibitors: the cell-permeative decanoyl-RVKR-chloromethylketone (cmk; 50 mM; 4026850.001; Bachem) and the cell surface PC inhibitor hexa-D-arginine (D6R; 20 μM; 344931; EMD). Culture media were then replaced with fresh ones containing the inhibitors for an additional 24 h. For the selective cell-permeative furin-like inhibitors (BOS; Boston Pharmaceuticals), the cells were treated with the inhibitors at the specified concentration starting at 5 h pretransfection and throughout the duration of the experiment.

Cell-to-cell fusion assay. HeLa or HeLa TZM-bl cells were plated at 200,000 in 12-well plates. HeLa cells were transiently transfected with different constructs of SARS-CoV-2 spike or NL4.3-HIV Env or an empty vector (V) and 0.2 μg of cytomegalovirus (CMV) Tat plasmid. HeLa TZM-bl cells were transfected with human ACE2, TMPRSS2, or a combination of both. At 6 h posttransfection, media were replaced with fresh ones containing furin inhibitors, and 24 h later, the cells were detached with PBS-EDTA (1 μM). Different combinations of HeLa and HeLa TZM-bl cells were placed in coculture plates at a ratio of 1:1 for a total of 60,000 cells/well of a 96-well place. After 18 to 24 h, the media were removed and 50 μL of cell lysis reagent was added in each well. Twenty microliters of the cell lysate was used for luciferase reading using 50 μL of *Renilla* luciferase reagent (Promega, Madison, WI). Relative light units (RLU)

were measured using a Promega GloMax plate reader and values were reported as fold increase over the RLU measured in coculture of HeLa cells transfected with an empty vector with respective TZM-bl cells.

Protein immunoprecipitation from coculture media. When indicated, a secreted form of doubly tagged spike-glycoprotein of SARS-CoV-2 (N-terminal HA tag and C-terminal V5 tag) from media of cocultured HeLa and HeLa-TZM-bl cells was analyzed by immunoprecipitation. Namely, 0.3 mL of media were precipitated with 25 μL of EZ view red anti-HA affinity gel (E 6779; Sigma-Aldrich) according to the manufacturer's protocol. Upon SDS-PAGE separation and PVDF transfer, the proteins were detected using an HA-HRP antibody (12-013-819; 1:3,500; Roche).

Microscopy. In our luciferase assay, cell cocultures were plated on glass coverslips. After 18 to 24 h, the cells were incubated with 488 CellMask to stain the membrane and then fixed with 4% paraformaldehyde (PFA) for 15 min at 4°C. The glass coverslips were mounted on glass slides using ProLong Gold antifade containing 4′,6-diamidino-2-phenylindole (DAPI; Invitrogen). The number of syncytia was counted over 10 fields.

Pseudovirus entry. HEK293T-ACE2 or Calu-3 cells (10,000 cells/well plated in a 96-well dish 24 or 48 h before, respectively) were incubated with up to 200 μL of filtered pseudovirions overnight. In certain experiments, target cells were pretreated with BOS-318 (1 μM) for 6 h and/or camostat (40 μM) for 2 h before transduction. The overnight incubation with pseudovirions was performed in the presence of the inhibitors. Viral inoculum was removed, then fresh media were added, and the cells were cultured for up to 72 h. Upon removal of spent media, 293T-ACE2 and Calu-3 cells were gently washed twice with PBS and analyzed for firefly luciferase or nanoluciferase activity, respectively, using the Promega luciferase assay (catalog no. E1501) or Nano-Glo luciferase system (catalog no. N1110), respectively.

Replication-competent SARS-CoV-2. SARS-CoV-2, which served as the viral source, was originally isolated from a COVID-19 patient in QC, Canada, and was designated LSPQ1. The clinical isolate was amplified, the titer was determined in Vero E6 cells using a plaque assay as detailed below, and the integrity of the S protein multibasic protein convertase site was validated by sequencing. All experiments involving infectious SARS-CoV-2 were performed in the designated areas of the biosafety level 3 laboratory (at IRCM) previously approved for SARS-CoV-2 work.

Plaque assay in Vero E6 cells. Vero E6 cells (1.2×10^5/well) were seeded in quadruplicate in 24-well tissue culture plates in DMEM supplemented with 10% FBS 2 days before infection. Cells were infected with up to six 10-fold serial dilutions (10^{-2} to 10^{-6}) of viral supernatant containing SARS-CoV-2 for 1 h at 37°C (200-μL infection volume). The plates were manually rocked every 15 min during the 1-h period. Subsequently, virus was removed, cells were washed, and overlaying medium (containing 0.6% low-melt agarose in DMEM with 10% FBS) was added and incubated undisturbed for 60 to 65 h at 37°C. After incubation, cells were fixed with 4% formaldehyde and stained with 0.25% crystal violet (prepared in 30% methanol). High-quality plaque pictures were taken using a high-resolution DLSR camera (Nikon; model D80; objective, AF Micro-Nikkor 60 mm f/2.8D). Plaques were counted manually and in parallel, imaged plaque plates were processed, and plaques were enumerated using an automated algorithm-based Matlab software, as previously reported (54). In brief, the program assigned a color to every object and each individual plaque was arbitrarily given a color shade, while fused plaques received one single color. The gray background depicts fields of live/uninfected cells (no plaques). Enumeration of plaques was done with at least two dilutions where individual/unfused plaques were observed. Virus titer is expressed as PFU per milliliter, determined as follows: (number of plaques $\times$ dilution factor of the virus) $\times$ 1,000/volume of virus dilution used for infection (in microliters). The multiplicity of infection (MOI) is expressed as PFU of virus used for infection/number of cells.

Cell infections with fully replicative SARS-CoV-2. Vero E6 and Calu-3 cells were seeded in duplicates in 12-well plates (2.3×10^5 cells/well) the day before. Cells were pretreated with various concentrations (0.1 to 1 μM) of BOS inhibitors and vehicle alone (DMSO) for up to 24 h. In certain experiments, Calu-3 cells were also pretreated with camostat for 1 h. Thereafter, cells were infected with SARS-CoV-2 at an MOI of 0.001 for 1 h (Vero E6) or 0.01 for 3h (Calu-3 cells) in 350 μL of serum-free DMEM at 37°C with occasional manual rocking of plates. Cells plus media only were used as a control. After incubation, virus was removed, and the cell monolayer was washed twice successively with PBS and serum-free DMEM. New media (total 1 mL) containing the concentrations of BOS inhibitors was subsequently added to cells. Cell-free supernatant (250 μL) was removed at 12, 24, and 48 h postinfection. The drugs were replenished for 1 mL of media at 24 h postinfection. The virus supernatants were stored at -80°C until further use. Viral production in the supernatant was quantified using a plaque assay on Vero E6.1 cells as described above. In certain experiments, viral supernatants were harvested at the end of infection and purified on a 20% sucrose cushion using ultracentrifugation as described above. The resulting concentrated virus and corresponding infected cells were analyzed by Western blotting as appropriate.

Quantification and statistical analysis. Virus titers quantified by plaque assay in triplicate are shown as means $\pm$ standard deviations. The results from experiments done with two biological replicates and two technical replicates in triplicates were used to calculate the IC_{50} by nonlinear regression using GraphPad Prism v5.0 software. The differences between the control cells (virus with 0.001% DMSO) and the cells treated with BOS inhibitors were evaluated by Student's *t* test. *P* values of 0.05 or lower were considered statistically significant (in figures, *P* values are represented as follows: *, $P < 0.05$; **, $P < 0.01$; ***, $P < 0.001$ and ****, $P < 0.0001$).

Data availability. Source data are provided with this paper. The data that support the findings of this study are preserved at repositories of the Montreal Clinical Research Institute (IRCM), Montreal, QC, Canada, and available from the corresponding authors upon reasonable request.

ACKNOWLEDGMENTS

This work was supported in part by CIHR Foundation grants (no. 148363 to N.G.S. and (no. 154324 to É.A.C.), a Canada Research Chair in Precursor Proteolysis (no. 950-231335 to N.G.S.), a CIHR CHAMPS Team Grant (no. HAL 157986 to N.G.S. and É.A.C.), Réseau SIDA maladies infectieuses COVID-19 initiative (to É.A.C. and N.G.S.), the European score project, and ANR Reacting COVID-19 (E.D. and B.C.). J.J. is supported by the CIHR Postdoctoral Fellowship (HIV-435243-73284).

We thank the Quebec public health laboratory for providing the infectious isolate LSPQ1 SARS-CoV-2. We thank Paul Bieniasz for the 293T-ACE2 cell line and the pHIV-1NL4-3ΔEnv-NanoLuc construct. The following reagents were obtained from the NIH AIDS Reagent Program, Division of AIDS, NIAID, NIH: TZM-bl cells, from John C. Kappes, Xiaoyun Wu, and Tranzyme, Inc., and HIV-1 pNL4-3 ΔEnv Vpr luciferase reporter vector (pNL4-3.Luc.R-E-), obtained from Nathaniel Landau. We are thankful to Dominic Filion for developing the algorithm for image-assisted plaque quantification. We also thank Ann Chamberland for qPCR analyses and Annik Prat (IRCM) for the design of the summary model shown in Fig. 12. Finally, we thank Habiba Oueslati and Brigitte Mary for their excellent editorial help and organization of the manuscript.

R.E. made all the original critical experiments revealing the role of the PCs in spike processing and the effect of their inhibitors. J.J. and T.NQ.P. performed all the cell assays with infectious SARS-CoV-2. D.S.-R. participated in the biochemical characterizations of TMPRSS2 processing of ACE2 and S1. U.A. performed all cell-to-cell fusion assays. A.E. made all the mutants used in the work. R.M.D. generated the HeLa-ACE2 cells and prepared all the cells for *ex vivo* analyses. D.N.H. performed all the immunocytochemical experiments. T.NQ.P., F.D., and M.L. performed experiments related to SARS-CoV-2 pseudovirions. A.D. and P.S.-O. performed all the furin and TMPRSS2 *in vitro* kinetic cleavage analyses of peptides mimicking the S1/S2 and S2′ sites. C.M. and K.W. provided the BOS inhibitors and their characterization. E.D. made seminal contributions to the possible role of furin-like enzymes in the processing of the spike glycoprotein and actively contributed to the conceptualization and writing of the manuscript. T.NQ.P. designed, performed, and analyzed experiments related to viral entry and contributed to the writing of the manuscript. É.A.C. (virology) and N.G.S. (biochemistry and cell biology) conceptualized the research program and provided the intellectual contributions and funding for the whole project. All authors actively contributed to the final version of the manuscript.

The Montreal Clinical Research Institute (IRCM) is affiliated with the University of Montreal.

REFERENCES

1. Cui J, Li F, Shi ZL. 2019. Origin and evolution of pathogenic coronaviruses. Nat Rev Microbiol 17:181–192. https://doi.org/10.1038/s41579-018-0118-9.
2. Belouzard S, Millet JK, Licitra BN, Whittaker GR. 2012. Mechanisms of coronavirus cell entry mediated by the viral spike protein. Viruses 4:1011–1033. https://doi.org/10.3390/v4061011.
3. Liu PP, Blet A, Smyth D, Li H. 2020. The science underlying COVID-19: implications for the cardiovascular system. Circulation 142:68–78. https://doi.org/10.1161/CIRCULATIONAHA.120.047549.
4. Usul Afsar C. 2020. 2019-nCoV-SARS-CoV-2 (COVID-19) infection: cruciality of furin and relevance with cancer. Med Hypotheses 140:109770. https://doi.org/10.1016/j.mehy.2020.109770.
5. Braun E, Sauter D. 2019. Furin-mediated protein processing in infectious diseases and cancer. Clin Transl Immunology 8:e1073. https://doi.org/10.1002/cti2.1073.
6. Izaguirre G. 2019. The proteolytic regulation of virus cell entry by furin and other proprotein convertases. Viruses 11:837. https://doi.org/10.3390/v11090837.
7. Seidah NG, Pasquato A, Andreo U. 2021. How do enveloped viruses exploit the secretory proprotein convertases to regulate infectivity and spread? Viruses 13:1229. https://doi.org/10.3390/v13071229.
8. Coutard B, Valle C, de Lamballerie X, Canard B, Seidah NG, Decroly E. 2020. The spike glycoprotein of the new coronavirus 2019-nCoV contains a furin-like cleavage site absent in CoV of the same clade. Antiviral Res 176:104742. https://doi.org/10.1016/j.antiviral.2020.104742.
9. Tang T, Bidon M, Jaimes JA, Whittaker GR, Daniel S. 2020. Coronavirus membrane fusion mechanism offers as a potential target for antiviral development. Antiviral Res 178:104792. https://doi.org/10.1016/j.antiviral.2020.104792.
10. Hoffmann M, Kleine-Weber H, Pöhlmann S. 2020. A multibasic cleavage site in the spike protein of SARS-CoV-2 is essential for infection of human lung cells. Mol Cell 78:779–784.e5. https://doi.org/10.1016/j.molcel.2020.04.022.
11. Xia S, Lan Q, Su S, Wang X, Xu W, Liu Z, Zhu Y, Wang Q, Lu L, Jiang S. 2020. The role of furin cleavage site in SARS-CoV-2 spike protein-mediated membrane fusion in the presence or absence of trypsin. Signal Transduct Target Ther 5:92. https://doi.org/10.1038/s41392-020-0184-0.
12. Johnson BA, Xie X, Bailey AL, Kalveram B, Lokugamage KG, Muruato A, Zou J, Zhang X, Juelich T, Smith JK, Zhang L, Bopp N, Schindewolf C, Vu M, Vanderheiden A, Winkler ES, Swetnam D, Plante JA, Aguilar P, Plante KS, Popov V, Lee B, Weaver SC, Suthar MS, Routh AL, Ren P, Ku Z, An Z, Debbink K, Diamond MS, Shi PY, Freiberg AN, Menachery VD. 2021. Loss of furin cleavage site attenuates SARS-CoV-2 pathogenesis. Nature 591:293–299. https://doi.org/10.1038/s41586-021-03237-4.

13. Peacock TP, Goldhill DH, Zhou J, Baillon L, Frise R, Swann OC, Kugathasan R, Penn R, Brown JC, Sanchez-David RY, Braga L, Williamson MK, Hassard JA, Staller E, Hanley B, Osborn M, Giacca M, Davidson AD, Matthews DA, Barclay WS. 2021. The furin cleavage site in the SARS-CoV-2 spike protein is required for transmission in ferrets. Nat Microbiol 6:899–909. https://doi.org/10.1038/s41564-021-00908-w.
14. Lan J, Ge J, Yu J, Shan S, Zhou H, Fan S, Zhang Q, Shi X, Wang Q, Zhang L, Wang X. 2020. Structure of the SARS-CoV-2 spike receptor-binding domain bound to the ACE2 receptor. Nature 581:215–220. https://doi.org/10.1038/s41586-020-2180-5.
15. Lu G, Wang Q, Gao GF. 2015. Bat-to-human: spike features determining 'host jump' of coronaviruses SARS-CoV, MERS-CoV, and beyond. Trends Microbiol 23:468–478. https://doi.org/10.1016/j.tim.2015.06.003.
16. Millet JK, Whittaker GR. 2018. Physiological and molecular triggers for SARS-CoV membrane fusion and entry into host cells. Virology 517:3–8. https://doi.org/10.1016/j.virol.2017.12.015.
17. Ou X, Liu Y, Lei X, Li P, Mi D, Ren L, Guo L, Guo R, Chen T, Hu J, Xiang Z, Mu Z, Chen X, Chen J, Hu K, Jin Q, Wang J, Qian Z. 2020. Characterization of spike glycoprotein of SARS-CoV-2 on virus entry and its immune cross-reactivity with SARS-CoV. Nat Commun 11:1620. https://doi.org/10.1038/s41467-020-15562-9.
18. Shang J, Wan Y, Luo C, Ye G, Geng Q, Auerbach A, Li F. 2020. Cell entry mechanisms of SARS-CoV-2. Proc Natl Acad Sci U S A 117:11727–11734. https://doi.org/10.1073/pnas.2003138117.
19. Bestle D, Heindl MR, Limburg H, Van Lam van T, Pilgram O, Moulton H, Stein DA, Hardes K, Eickmann M, Dolnik O, Rohde C, Klenk HD, Garten W, Steinmetzer T, Böttcher-Friebertshäuser E. 2020. TMPRSS2 and furin are both essential for proteolytic activation of SARS-CoV-2 in human airway cells. Life Sci Alliance 3:e202000786. https://doi.org/10.26508/lsa.202000786.
20. Mykytyn AZ, Breugem TI, Riesebosch S, Schipper D, van den Doel PB, Rottier RJ, Lamers MM, Haagmans BL. 2021. SARS-CoV-2 entry into human airway organoids is serine protease-mediated and facilitated by the multibasic cleavage site. Elife 10:e64508. https://doi.org/10.7554/eLife.64508.
21. Seidah NG, Prat A. 2012. The biology and therapeutic targeting of the proprotein convertases. Nat Rev Drug Discov 11:367–383. https://doi.org/10.1038/nrd3699.
22. Van de Ven WJ, Creemers JW, Roebroek AJ. 1991. Furin: the prototype mammalian subtilisin-like proprotein-processing enzyme. Endoproteolytic cleavage at paired basic residues of proproteins of the eukaryotic secretory pathway. Enzyme 45:257–270. https://doi.org/10.1159/000468900.
23. Moulard M, Decroly E. 2000. Maturation of HIV envelope glycoprotein precursors by cellular endoproteases. Biochim Biophys Acta 1469:121–132. https://doi.org/10.1016/s0304-4157(00)00014-9.
24. Millet JK, Whittaker GR. 2015. Host cell proteases: critical determinants of coronavirus tropism and pathogenesis. Virus Res 202:120–134. https://doi.org/10.1016/j.virusres.2014.11.021.
25. Afar DE, Vivanco I, Hubert RS, Kuo J, Chen E, Saffran DC, Raitano AB, Jakobovits A. 2001. Catalytic cleavage of the androgen-regulated TMPRSS2 protease results in its secretion by prostate and prostate cancer epithelia. Cancer Res 61:1686–1692.
26. Shrimp JH, Kales SC, Sanderson PE, Simeonov A, Shen M, Hall MD. 2020. An enzymatic TMPRSS2 assay for assessment of clinical candidates and discovery of inhibitors as potential treatment of COVID-19. ACS Pharmacol Transl Sci 3:997–1007. https://doi.org/10.1021/acsptsci.0c00106.
27. Kawase M, Shirato K, van der Hoek L, Taguchi F, Matsuyama S. 2012. Simultaneous treatment of human bronchial epithelial cells with serine and cysteine protease inhibitors prevents severe acute respiratory syndrome coronavirus entry. J Virol 86:6537–6545. https://doi.org/10.1128/JVI.00094-12.
28. Nimishakavi S, Raymond WW, Gruenert DC, Caughey GH. 2015. Divergent inhibitor susceptibility among airway lumen-accessible tryptic proteases. PLoS One 10:e0141169. https://doi.org/10.1371/journal.pone.0141169.
29. Hörnich BF, Großkopf AK, Schlagowski S, Tenbusch M, Kleine-Weber H, Neipel F, Stahl-Hennig C, Hahn AS. 2021. SARS-CoV-2 and SARS-CoV spike-mediated cell-cell fusion differ in the requirements for receptor expression and proteolytic activation. J Virol 95:e00002-21. https://doi.org/10.1128/JVI.00002-21.
30. Hoffmann M, Kleine-Weber H, Schroeder S, Kruger N, Herrler T, Erichsen S, Schiergens TS, Herrler G, Wu NH, Nitsche A, Muller MA, Drosten C, Pohlmann S. 2020. SARS-CoV-2 cell entry depends on ACE2 and TMPRSS2 and is blocked by a clinically proven protease inhibitor. Cell 181:271–280.e8. https://doi.org/10.1016/j.cell.2020.02.052.
31. Cyranoski D. 2020. Profile of a killer: the complex biology powering the coronavirus pandemic. Nature 581:22–26. https://doi.org/10.1038/d41586-020-01315-7.
32. Matoba Y, Aoki Y, Tanaka S, Yahagi K, Katsushima Y, Katsushima F, Sugawara K, Matsuzaki Y, Mizuta K. 2016. HeLa-ACE2-TMPRSS2 cells are useful for the isolation of human coronavirus 229E. Jpn J Infect Dis 69:452–454. https://doi.org/10.7883/yoken.JJID.2016.106.
33. Thomas G. 2002. Furin at the cutting edge: from protein traffic to embryogenesis and disease. Nat Rev Mol Cell Biol 3:753–766. https://doi.org/10.1038/nrm934.
34. Örd M, Faustova I, Loog M. 2020. Biochemical evidence of furin specificity and potential for phospho-regulation at Spike protein S1/S2 cleavage site in SARS-CoV2 but not in SARS-CoV1 or MERS-CoV. bioRxiv. https://doi.org/10.1101/2020.06.23.166900.
35. Andersen KG, Rambaut A, Lipkin WI, Holmes EC, Garry RF. 2020. The proximal origin of SARS-CoV-2. Nat Med 26:450–452. https://doi.org/10.1038/s41591-020-0820-9.
36. Schjoldager KT, Clausen H. 2012. Site-specific protein O-glycosylation modulates proprotein processing—deciphering specific functions of the large polypeptide GalNAc-transferase gene family. Biochim Biophys Acta 1820:2079–2094. https://doi.org/10.1016/j.bbagen.2012.09.014.
37. Yu S, Zheng X, Zhou B, Li J, Chen M, Deng R, Wong G, Lavillette D, Meng G. 2022. SARS-CoV-2 spike engagement of ACE2 primes S2′ site cleavage and fusion initiation. Proc Natl Acad Sci U S A 119:e2111199119. https://doi.org/10.1073/pnas.2111199119.
38. Benton DJ, Wrobel AG, Xu P, Roustan C, Martin SR, Rosenthal PB, Skehel JJ, Gamblin SJ. 2020. Receptor binding and priming of the spike protein of SARS-CoV-2 for membrane fusion. Nature 588:327–330. https://doi.org/10.1038/s41586-020-2772-0.
39. Belouzard S, Chu VC, Whittaker GR. 2009. Activation of the SARS coronavirus spike protein via sequential proteolytic cleavage at two distinct sites. Proc Natl Acad Sci U S A 106:5871–5876. https://doi.org/10.1073/pnas.0809524106.
40. Hallenberger S, Bosch V, Angliker H, Shaw E, Klenk HD, Garten W. 1992. Inhibition of furin-mediated cleavage activation of HIV-1 glycoprotein gp160. Nature 360:358–361. https://doi.org/10.1038/360358a0.
41. Susan-Resiga D, Essalmani R, Hamelin J, Asselin MC, Benjannet S, Chamberland A, Day R, Szumska D, Constam D, Bhattacharya S, Prat A, Seidah NG. 2011. Furin is the major processing enzyme of the cardiac-specific growth factor bone morphogenetic protein 10. J Biol Chem 286:22785–22794. https://doi.org/10.1074/jbc.M111.233577.
42. Cheng YW, Chao TL, Li CL, Chiu MF, Kao HC, Wang SH, Pang YH, Lin CH, Tsai YM, Lee WH, Tao MH, Ho TC, Wu PY, Jang LT, Chen PJ, Chang SY, Yeh SH. 2020. Furin inhibitors block SARS-CoV-2 spike protein cleavage to suppress virus production and cytopathic effects. Cell Rep 33:108254. https://doi.org/10.1016/j.celrep.2020.108254.
43. Walls AC, Park YJ, Tortorici MA, Wall A, McGuire AT, Veesler D. 2020. Structure, function, and antigenicity of the SARS-CoV-2 spike glycoprotein. Cell 181:281–292.e6. https://doi.org/10.1016/j.cell.2020.02.058.
44. Hoffmann M, Mösbauer K, Hofmann-Winkler H, Kaul A, Kleine-Weber H, Krüger N, Gassen NC, Müller MA, Drosten C, Pöhlmann S. 2020. Chloroquine does not inhibit infection of human lung cells with SARS-CoV-2. Nature 585:588–590. https://doi.org/10.1038/s41586-020-2575-3.
45. Vincent MJ, Bergeron E, Benjannet S, Erickson BR, Rollin PE, Ksiazek TG, Seidah NG, Nichol ST. 2005. Chloroquine is a potent inhibitor of SARS coronavirus infection and spread. Virol J 2:69. https://doi.org/10.1186/1743-422X-2-69.
46. Bayati A, Kumar R, Francis V, McPherson PS. 2021. SARS-CoV-2 infects cells following viral entry via clathrin-mediated endocytosis. J Biol Chem 296:100306. https://doi.org/10.1016/j.jbc.2021.100306.
47. Platt EJ, Wehrly K, Kuhmann SE, Chesebro B, Kabat D. 1998. Effects of CCR5 and CD4 cell surface concentrations on infections by macrophagetropic isolates of human immunodeficiency virus type 1. J Virol 72:2855–2864. https://doi.org/10.1128/JVI.72.4.2855-2864.1998.
48. Plante JA, Mitchell BM, Plante KS, Debbink K, Weaver SC, Menachery VD. 2021. The variant gambit: COVID-19's next move. Cell Host Microbe 29:508–515. https://doi.org/10.1016/j.chom.2021.02.020.
49. Peacock TP, Penrice-Randal R, Hiscox JA, Barclay WS. 2021. SARS-CoV-2 one year on: evidence for ongoing viral adaptation. J Gen Virol 102:001584. https://doi.org/10.1099/jgv.0.001584.
50. Rajah MM, Hubert M, Bishop E, Saunders N, Robinot R, Grzelak L, Planas D, Dufloo J, Gellenoncourt S, Bongers A, Zivaljic M, Planchais C, Guivel-Benhassine F, Porrot F, Mouquet H, Chakrabarti LA, Buchrieser J, Schwartz O. 2021. SARS-CoV-2 Alpha, Beta, and Delta variants display enhanced spike-mediated syncytia formation. EMBO J 40:e108944. https://doi.org/10.15252/embj.2021108944.

51. Heurich A, Hofmann-Winkler H, Gierer S, Liepold T, Jahn O, Pöhlmann S. 2014. TMPRSS2 and ADAM17 cleave ACE2 differentially and only proteolysis by TMPRSS2 augments entry driven by the severe acute respiratory syndrome coronavirus spike protein. J Virol 88:1293–1307. https://doi.org/10.1128/JVI.02202-13.
52. Matsuyama S, Nagata N, Shirato K, Kawase M, Takeda M, Taguchi F. 2010. Efficient activation of the severe acute respiratory syndrome coronavirus spike protein by the transmembrane protease TMPRSS2. J Virol 84:12658–12664. https://doi.org/10.1128/JVI.01542-10.
53. Monteil V, Kwon H, Prado P, Hagelkrüys A, Wimmer RA, Stahl M, Leopoldi A, Garreta E, Hurtado Del Pozo C, Prosper F, Romero JP, Wirnsberger G, Zhang H, Slutsky AS, Conder R, Montserrat N, Mirazimi A, Penninger JM. 2020. Inhibition of SARS-CoV-2 infections in engineered human tissues using clinical-grade soluble human ACE2. Cell 181:905–913.e7. https://doi.org/10.1016/j.cell.2020.04.004.
54. Bellamine A, Pham TNQ, Jain J, Wilson J, Sahin K, Dallaire F, Seidah NG, Durkee S, Radošević K, Cohen ÉA. 2021. L-carnitine tartrate downregulates the ACE2 receptor and limits SARS-CoV-2 infection. Nutrients 13:1297. https://doi.org/10.3390/nu13041297.
55. Altulea D, Maassen S, Baranov MV, van den Bogaart G. 2021. What makes (hydroxy)chloroquine ineffective against COVID-19: insights from cell biology. J Mol Cell Biol 13:175–184. https://doi.org/10.1093/jmcb/mjab016.
56. Glowacka I, Bertram S, Müller MA, Allen P, Soilleux E, Pfefferle S, Steffen I, Tsegaye TS, He Y, Gnirss K, Niemeyer D, Schneider H, Drosten C, Pöhlmann S. 2011. Evidence that TMPRSS2 activates the severe acute respiratory syndrome coronavirus spike protein for membrane fusion and reduces viral control by the humoral immune response. J Virol 85:4122–4134. https://doi.org/10.1128/JVI.02232-10.
57. Raghuvamsi PV, Tulsian NK, Samsudin F, Qian X, Purushotorman K, Yue G, Kozma MM, Hwa WY, Lescar J, Bond PJ, MacAry PA, Anand GS. 2021. SARS-CoV-2 S protein:ACE2 interaction reveals novel allosteric targets. Elife 10:e63646. https://doi.org/10.7554/eLife.63646.
58. Zhang H, Wada J, Hida K, Tsuchiyama Y, Hiragushi K, Shikata K, Wang H, Lin S, Kanwar YS, Makino H. 2001. Collectrin, a collecting duct-specific transmembrane glycoprotein, is a novel homolog of ACE2 and is developmentally regulated in embryonic kidneys. J Biol Chem 276:17132–17139. https://doi.org/10.1074/jbc.M006723200.
59. Yan R, Zhang Y, Li Y, Xia L, Guo Y, Zhou Q. 2020. Structural basis for the recognition of SARS-CoV-2 by full-length human ACE2. Science 367:1444–1448. https://doi.org/10.1126/science.abb2762.
60. Yamamoto M, Kiso M, Sakai-Tagawa Y, Iwatsuki-Horimoto K, Imai M, Takeda M, Kinoshita N, Ohmagari N, Gohda J, Semba K, Matsuda Z, Kawaguchi Y, Kawaoka Y, Inoue JI. 2020. The anticoagulant nafamostat potently inhibits SARS-CoV-2 S protein-mediated fusion in a cell fusion assay system and viral infection in vitro in a cell-type-dependent manner. Viruses 12:629. https://doi.org/10.3390/v12060629.
61. Koch J, Uckeley ZM, Doldan P, Stanifer M, Boulant S, Lozach PY. 2021. TMPRSS2 expression dictates the entry route used by SARS-CoV-2 to infect host cells. EMBO J 40:e107821. https://doi.org/10.15252/embj.2021107821.
62. Wölfel R, Corman VM, Guggemos W, Seilmaier M, Zange S, Müller MA, Niemeyer D, Jones TC, Vollmar P, Rothe C, Hoelscher M, Bleicker T, Brünink S, Schneider J, Ehmann R, Zwirglmaier K, Drosten C, Wendtner C. 2020. Virological assessment of hospitalized patients with COVID-2019. Nature 581:465–469. https://doi.org/10.1038/s41586-020-2196-x.
63. Zhou L, Niu Z, Jiang X, Zhang Z, Zheng Y, Wang Z, Zhu Y, Gao L, Huang H, Wang X, Sun Q. 2020. The SARS-CoV-2 targets by the pscRNA profiling of ACE2, TMPRSS2 and furin proteases. iScience 23:101744. https://doi.org/10.1016/j.isci.2020.101744.
64. Mayer G, Boileau G, Bendayan M. 2004. Sorting of furin in polarized epithelial and endothelial cells: expression beyond the Golgi apparatus. J Histochem Cytochem 52:567–580. https://doi.org/10.1177/002215540405200502.
65. Antalis TM, Bugge TH, Wu Q. 2011. Membrane-anchored serine proteases in health and disease. Prog Mol Biol Transl Sci 99:1–50. https://doi.org/10.1016/B978-0-12-385504-6.00001-4.
66. Chu H, Chan JF-W, Yuen TT-T, Shuai H, Yuan S, Wang Y, Hu B, Yip CC-Y, Tsang JO-L, Huang X, Chai Y, Yang D, Hou Y, Chik KK-H, Zhang X, Fung AY-F, Tsoi H-W, Cai J-P, Chan W-M, Ip JD, Chu AW-H, Zhou J, Lung DC, Kok K-H, To KK-W, Tsang OT-Y, Chan K-H, Yuen K-Y. 2020. Comparative tropism, replication kinetics, and cell damage profiling of SARS-CoV-2 and SARS-CoV with implications for clinical manifestations, transmissibility, and laboratory studies of COVID-19: an observational study. Lancet Microbe 1:e14–e23. https://doi.org/10.1016/S2666-5247(20)30004-5.
67. Gunst JD, Staerke NB, Pahus MH, Kristensen LH, Bodilsen J, Lohse N, Dalgaard LS, Brønnum D, Fröbert O, Hønge B, Johansen IS, Monrad I, Erikstrup C, Rosendal R, Vilstrup E, Mariager T, Bove DG, Offersen R, Shakar S, Cajander S, Jørgensen NP, Sritharan SS, Breining P, Jespersen S, Mortensen KL, Jensen ML, Kolte L, Frattari GS, Larsen CS, Storgaard M, Nielsen LP, Tolstrup M, Sædder EA, Østergaard LJ, Ngo HTT, Jensen MH, Højen JF, Kjolby M, Søgaard OS. 2021. Efficacy of the TMPRSS2 inhibitor camostat mesilate in patients hospitalized with Covid-19—a double-blind randomized controlled trial. EClinicalMedicine 35:100849. https://doi.org/10.1016/j.eclinm.2021.100849.
68. Shapira T, Monreal IA, Dion SP, Jager M, Désilets A, Olmstead AD, Vandal T, Buchholz DW, Imbiakha B, Gao G, Chin A, Rees WD, Steiner T, Nabi IR, Marsault E, Sahler J, August A, Van de Walle G, Whittaker GR, Boudreault PL, Aguilar HC, Leduc R, Jean F. 2021. A novel highly potent inhibitor of TMPRSS2-like proteases blocks SARS-CoV-2 variants of concern and is broadly protective against infection and mortality in mice. bioRxiv. https://doi.org/10.1101/2021.05.03.442520.
69. Ou T, Mou H, Zhang L, Ojha A, Choe H, Farzan M. 2021. Hydroxychloroquine-mediated inhibition of SARS-CoV-2 entry is attenuated by TMPRSS2. PLoS Pathog 17:e1009212. https://doi.org/10.1371/journal.ppat.1009212.
70. Morens DM, Fauci AS. 2020. Emerging pandemic diseases: how we got to COVID-19. Cell 183:837. https://doi.org/10.1016/j.cell.2020.10.022.
71. Lodge R, Lalonde JP, Lemay G, Cohen EA. 1997. The membrane-proximal intracytoplasmic tyrosine residue of HIV-1 envelope glycoprotein is critical for basolateral targeting of viral budding in MDCK cells. EMBO J 16:695–705. https://doi.org/10.1093/emboj/16.4.695.
72. Forget J, Yao XJ, Mercier J, Cohen EA. 1998. Human immunodeficiency virus type 1 vpr protein transactivation function: mechanism and identification of domains involved. J Mol Biol 284:915–923. https://doi.org/10.1006/jmbi.1998.2206.
73. Schmidt F, Weisblum Y, Muecksch F, Hoffmann HH, Michailidis E, Lorenzi JCC, Mendoza P, Rutkowska M, Bednarski E, Gaebler C, Agudelo M, Cho A, Wang Z, Gazumyan A, Cipolla M, Caskey M, Robbiani DF, Nussenzweig MC, Rice CM, Hatziioannou T, Bieniasz PD. 2020. Measuring SARS-CoV-2 neutralizing antibody activity using pseudotyped and chimeric viruses. J Exp Med 217:e20201181. https://doi.org/10.1084/jem.20201181.
74. Dubuc G, Chamberland A, Wassef H, Davignon J, Seidah NG, Bernier L, Prat A. 2004. Statins upregulate PCSK9, the gene encoding the proprotein convertase neural apoptosis-regulated convertase-1 implicated in familial hypercholesterolemia. Arterioscler Thromb Vasc Biol 24:1454–1459. https://doi.org/10.1161/01.ATV.0000134621.14315.43.